SAND2019-5559J

Technique for inferring angle change as a function of time for high-current electron beams using a dose-rate monitor array

T. J. Renk[1], B. V. Weber[2], I. M. Rittersdorf[2], and T. J. Webb[1]

[1]Sandia National Laboratories, Albuquerque, NM 87185

[2]Plasma Physics Division, Naval Research Laboratory, Washington, DC 20375

ABSTRACT

Intense electron beams striking a high-atomic number target produce high-output pulsed photon fluxes for flash x-ray experiments. Without an external guide field, such beams are subject to dynamics of high-current electron beam propagation, including changes to electron trajectories either from self-fields, or from development of beam instabilities. Bremsstrahlung output (dose-rate) scales approximately as IV^x, where I is the beam current, V the electron energy, and where x is generally described as being in the 2.0 – 2.65 range, and depends upon the electron angle on the converter. Using experimental beam data (dose-rate, I and V), this equation can be solved for x, a process known as "inverting the Radiographer's Equation". Inversion methods that rely on thermoluminescent dosimeters (TLDs), which are time-integrated, yield no information about evolution of the electron beam angle in time. We propose here a different inversion method based upon deployment of several dose-rate monitors at different angles with respect to the beam axis. By measuring dose-rates at different angles, one can infer the time-dependent beam voltage and angle. This method compares well with estimates of corrected voltage and results in a self-consistent picture of beam dynamics.

Key words: intense electron beams, inductive voltage adder (IVA) accelerators, dose-rate diagnostics, high-current electron beam focusing

I. INTRODUCTION

Pulsed intense electron beams are well-known as a source of pulsed high-output x-rays, produced via the bremsstrahlung process. An electron beam impinges on a planar target, and as a result a fraction of the electron energy is converted to a burst of high-energy photons. It is of interest to maximize the production of such photons, and considerable research work has been undertaken over a period of decades to both characterize and optimize the x-ray output for a given electron beam source. Since a typical object of interest for exposure to such pulsed photon fluences is located on or near the beam propagation axis, photon flux in the forward (axial) direction is of primary importance. For relativistic beam energies, the forward bias of the emitted photons (which increases with beam energy) aids in this effort. In the case of the RITS-6 experiments described in this paper, the peak voltage encountered ranges from 4.5 MV to 8.5 MV, well into the relativistic regime for electrons.

Propagating electron beams are characterized by several parameters: 1) beam energy, determined from the accelerating voltage pulse as a function of time, 2) beam current (also as a function of time), and 3) angle of incidence of the electrons on the anode plane (bremsstrahlung target). Of these parameters, the beam current may be the easiest to measure. For example, in the case of the RITS-6[1] facility, the testbed for the diagnostics described here, the driver hardware consists of an Inductive Voltage Adder (IVA) delivering power through a magnetically insulated transmission line (MITL)[2] to a type of diode known as a Self-Magnetic Field Pinch (SMP)[1]. A schematic view including the diode region and the IVA section closest to it is shown in Fig. 1. In the MITL section, which consists of inner (cathode) and outer (anode) coaxial cylinders, there are sets of calibrated B-dot current monitors located along the propagation axis on both the inner and outer conductors. At each "X" in the Figure, signals from sets of 4 Bdots spaced azimuthally are time-integrated and averaged together to yield the current at that location. For negative polarity output, the inner (cathode) monitors measure the bound current (I_c), i.e. current flowing through the inner conductor, and the outer (anode) monitors measure the total current (I_a). The difference between the two yields the MITL flow current. In Fig. 1, inner and outer Bdots are located at Position G, and at two other locations (called Positions E and F) farther from the diode and out

of view. Using the I_c and I_a monitors, the amount of MITL flow current can be determined, and using I_c and I_a, the voltage at that location can be estimated using MITL flow theory[3-7]. The voltage and current are thus estimated at a point in the MITL near the diode load, and current monitors closer to the A-K gap can be used to inductively correct the voltage at G to the anode-cathode gap. This inductive correction uses the measured load current, and an estimate of the inductance between point G, at which the voltage is measured, and the diode load. In the case of RITS-6 SMP experiments, a description of this method has been previously described[1]. The accuracy with which the load current and voltage can be estimated in any given experiment thus depends upon the geometrical layout of the load region, and proximity of any additional current monitors between the upstream location and the load. An extended discussion of the use of Bdots in the determination of voltage and current in MITLs is given in Reference 8.

The most complex factor to consider for bremsstrahlung production by intense pulsed electron beams, once electron energy and current are estimated, is the dynamics of electron beam propagation to the target, and the interaction of electrons with the target. The dynamics are important to understand, and differ from low-current beams, because self-fields play an important role in beam propagation and interaction with the target. Beam interaction with the target is discussed first. Of the possible interactions (electron-electron and electron-nucleus), electron-nucleus interactions are by far the largest source of photon generation. This is inherently a three-body problem, and photon yield cross-section determinations require quantum-mechanical calculations. Details of such calculations are beyond the scope of this paper, except to say that for the electron energy range of most interest to bremsstrahlung researchers (~ 1 to 30 MeV), approximations made in the calculations (e.g. screened or unscreened nucleus) are the least reliable compared to < 1 MeV or > 50 MeV. Readers interested in further details are referred to an excellent summary in Reference 9, and further discussions in Reference 10. The comprehensive review of formulae and related data by Koch and Motz[11] has become the reference for bremsstrahlung cross-sections. Seltzer and Berger[12] later combined the available theories to derive differential bremsstrahlung cross-sections for electrons in the range 1 keV to 10 GeV incident on neutral atoms with atomic numbers Z = 1 to 100. The datasets so derived serve as a basis for bremsstrahlung photon production using the Monte Carlo method in such simulation codes as ETRAN[13], Integrated TIGER Series[14], and MCNP[15]. The modeling

discussion later in this paper concerns calculations conducted using CYLTRAN, a 2-dimensional code that is part of the Integrated TIGER Series.

Early validation experiments demonstrated that the basic theory governing electron-target interactions was physically realizable. In one such validation experiment series[16], a pencil electron beam of 20 μA current impinged upon various targets of thickness slightly thicker than the maximum electron range for the particular material. Photon fluence was investigated as a function of electron energy, atomic number of the target, the angle between the observation direction and the incident electron beam, and angle between the incident beam and the target. It was found that for a typical impinging electron energy of 2.35 MeV, photon fluence was strongly peaked in the forward direction, and increased with the target atomic number. The photon fluence scaling was also a function of the observation angle. The total photon energy radiated varied linearly with atomic number. For a gold target, an estimated 7.4% of the incident electron energy was converted to photon radiation (at 2.35 MeV). This compares favorably with an 8.3% estimate from the basic theory of Bethe and Heitler[17]. Given that the basic theory applies to only a single collision, not the multiple collision events occurring in a thick target interaction, this gives confidence that the complex theory of the bremsstrahlung process can be applied in a practical fielding geometry. The challenge for our purposes is in application of these results to high-current beams and complex detector geometries. For instance, if the electron beam incidence angle consists of a distribution of values instead of a single value, or if the incidence angle(s) change with time, how might that affect the observed dose-rate distribution over observation angles?

We return now to the consideration of the first part of the electron beam interaction with the target, that of the dynamics of the beam transport to the converter plane, including the current, current distribution, and electron trajectories to the converter. Koch and Motz, in analyzing the Buechner data, pointed out that the power radiated in the forward direction (that is, when the angle between the photon emission and electron strike angle on the converter is 0°, and the electron strikes the converter normal to its surface) scales like a rather large power of the electron kinetic energy. If we label the power as x, then for a gold target, x = 2.9, and for a

beryllium target x = 3.4. (The gold target still radiates more net photon power due to its higher atomic number.)

In the RITS experiments discussed here, the dose-rate measured by PIN detectors is the observable, rather than total radiated power. It is clear from the above discussion that mathematically, the scaling of emitted photon dose-rate is a larger power of voltage than current (which is linear). This dose-rate D can be approximated by the following form:

$$D = cIV^x \quad (1)$$

where I = current in Amperes, V = electron energy in MeV, and c is a constant. The factor x (hereafter known as the x-factor) depends upon the electron beam angle of incidence, the details of the x-ray converter materials, and the angle of observation. The form of (1) is referred to generically as a Radiographer's Equation[18], as it pertains to dose calculations relevant for the flash x-ray radiography application. Total photon dose can then be a function of the x-factor, electron energy and current, converter material and geometry, and any intervening radiation-absorbing material between the x-ray source and the radiation detector. The dependence of dose on electron strike angle leads to a much larger discussion about how the dose maximization objective differs in its physics from the model validation experiments discussed above. The electron strike angle was varied from 0 – 140° in the Buechner setup previously discussed, but for each strike angle chosen, the electron trajectory to the target remained constant during the period of observation. The kind of electron beams used in multi-MeV flash x-ray generation – intense pulsed beams – are characterized by strong self-magnetic fields that play a key role in beam propagation. As an example, consider an intense bremsstrahlung source such as that generated on the HERMES III accelerator (18 MV, 700 kA, 40 ns) at Sandia National Laboratories[19,20,21]. For bremsstrahlung experiments, the inner conductor of the HERMES IVA is terminated in an annular cathode, separated from the anode converter by a 53 cm anode-cathode (A-K) gap. The annular electron beam launched from the cathode (a mixture of flow plus electrons emitted from the annular cathode) expands slightly in radius, then propagates in an approximately axial direction, until it approaches within a few cm of the anode plane. The axial propagation represents a balance between electric and self-magnetic forces. However, the

(metallic) anode plane shorts out the radial electric field, leaving the self-magnetic field unbalanced. This results in the beam pinching inward as it strikes the anode converter. This is just one aspect of beam dynamics that can lead to changes in the electron angle. Other sources can be various beam instabilities caused when such an intense beam propagates in space, ion emission from the anode, and evolving electrode plasmas.

As for the SMP diode that is the subject of this paper, various forms of the Radiographer's Equation have been developed over time by different researchers. A number of these are discussed by Hahn[1]. All such equations make an assumption about the collective electron strike angles on the anode converter. One of the equations (by Crotch), developed from the MCNP radiation transport code, is in the form of a polynomial in V, and assumes a 0-40° fully filled cone of electrons incident on the converter. Another equation proposed by Hinshelwood *et al*[22] scales like Eq. 1 above with the x-factor = 2.2. This was based on Monte Carlo simulations using the ITS code, and assuming a mono-angular 20° electron-beam incident on the converter. Note that since 2.2 is a number significantly smaller than 2.9 (from Koch and Motz above), the use of intense electron beams with inward-pinching results in a reduction of the x-factor compared to lower-current diagnostic electron beams which can strike the anode plane at normal incidence.

Since the actual electron orbits in the SMP diode (or any diode for that matter) are not well known, these assumptions of collective electron angles (e.g., fully-filled cone or mono-angular) are mathematical constructs that allow for development of solutions that can be compared to measured dose or dose-rate. That is, the assumption of say 20° mono-angular electron angles should not be taken as suggesting that these are the actual electron trajectories, only that the electron population can be treated mathematically as behaving that way. We will take the same position in the discussions of the behavior of electron incidence angles later in this paper.

Whatever the x-factor value that is assumed in a given Radiographer's Equation, if one starts with the experimental value of the dose-rate, a variant of Eq. 1 can be solved for the diode voltage V, as already discussed. This is known as "inverting the Radiographer's Equation." Note, however, that this can only be done for a *fixed* value of x, e.g. it is assumed that the electron

angle(s) do not change during the power pulse. In the various references cited, the prospect of electron angles changing during the power pulse is not considered.

We present in this paper a technique for inferring electron angle changes during the power pulse, by, in effect, allowing the c and x-factor in Eq. 1 to change as functions of time. The technique is based on ITS modeling, and includes the use of several different dose-rate detectors located both on and off the radiation axis. As already noted, the variation in the x-factor depends upon both the angle at which the electrons strike the converter, and the observation angle of the radiation detector with respect to the diode axis. So for example, the x-factor in the forward direction is different from that in say the 45° direction. But in addition to this, as will be investigated below, there is the scaling of the x-factor in a particular observation direction *as the electron angle(s) to the converter change with time*. In these discussions, the angle at which the electrons strike the converter at normal incidence is defined as 0°. In the extreme case of 90° angle, electrons would approach the converter parallel to its surface. As the analysis below will show, while the x-factor in the forward direction decreases as the electron angle increases, the axis-factor in the 95° direction actually *increases* in response to the same electron angle increase. To our knowledge, this type of scaling has not been investigated before, because prior discussions of the Radiographer's Equation have not allowed for changes to the x-factor as a function of time. The ITS modeling can be combined with the calculated behavior of the diode voltage with time, and the resultant combination of two separate elements of data analysis can then result in a self-consistent picture of electron dynamics.

We will also show that this self-consistent picture of electron dynamics can range from qualitatively useful to a more quantitative picture, depending on how the experimental dose-rate data are consistent with the ITS modeling predictions in all observation directions. One example of the utility of this approach is that changes to the measured detector dose rate can be separated between those due to the electron angle changing, and those due to variation in the diode voltage.

The experimental setup of the RITS-6 SMP diode is described in Section II below, along with a description of the input setup for the ITS CYLTRAN modeling. Results of the CYLTRAN analysis are presented in Sections III and IV, along with examples of key observations of

electron dynamics in the RITS-6 SMP experiments. Summary and conclusions are left to Section V.

II. Geometry of the RITS-6 SMP diode and ITS modeling information

A. Description of RITS MITL and load region, calculation of corrected diode votage

A simplified diagram of the RITS-6 downstream MITL and SMP load region is shown in Figure 1. The inner MITL (gray) connects to the inductive voltage adder (IVA), out of view to the left. The outer MITL expands into a much larger chamber that contains the inner MITL field shaper and SMP diode load region. Near the point where the outer MITL expands, the inner MITL transitions to a cone structure, which then intersects a field shaper. The function of the field shaper is to divert the MITL electron flow away from the diode region. The cathode is connected to the downstream end of the field shaper, opposite the anode/converter. The red "X" marks indicate the general position of Bdot current monitors that measure current flow at different positions along the inner and outer conductors. At several positions along the MITL, including the position marked 'G', just before the outer MITL is attached to the larger-radius portion of the vacuum chamber, and two others out of view to the left, are a set of 4 Bdots equally spaced in azimuth on both the inner and outer conductors. From this location, the voltage coming forward towards the A-K region can be calculated using the theory of Miller and Mendel[4,5], as modified more recently[6,7]. The form of the Mendel Equation used for this paper is given by an expression from Reference 6:

$$V_{MITL} = Z_0(I_a^2 - I_c^2)^{1/2} - [(gmc^2/2e)(I_a^2 - I_c^2)/I_c^2] \qquad (2)$$

where I_a denotes the total current measured at a particular point in the MITL, I_c denotes the bound (cathode) current at the axial same location, Z_0 is the MITL vacuum impedance of the MITL, and g is a parameter of order 1. (If g = 1, the original Mendel equation is recovered.) The

value of g is determined from particle-in-cell (PIC) simulations, and for an output voltage of ~ 8 MV, g is determined to be ~ 0.8. Accordingly, this value of g is assumed for analyses in this paper. In practical terms, the difference between a g value of 1 and 0.8 amounts to ~ 0.2 MV difference in the calculated voltage.

Close to the cathode, there are a set of four Bdots. Their signals are time-integrated and averaged together and called "IBEAM". This gives an estimate of the load current (e.g. the electron current emitted from the cathode plus ion current emitted from the anode). The load voltage can be estimated by inductively correcting the voltage calculated at a given MITL position using Eq. 2 and IBEAM and the inductance L between the MITL position and load using the formula

$$V_{CORR} = V_{MITL} - L\,dIBEAM/dt \qquad (3)$$

A discussion of the use of this formula, as well as a more detailed discussion of the RITS SMP diode and MITL region is given in Reference 1. It should be pointed out here that while Eq. 3 gives a mathematical prescription for calculating V_{CORR}, the formula contains several assumptions that may not be correct for the entire power pulse. V_{MITL}, for instance, is time-shifted to the diode position, typically ~ 7 ns, leading to the implicit assumption that the forward-going voltage remains unchanged from the MITL position to the diode load. And V_{MITL} itself is determined from the forward-going currents (through Eq. 2), which are assumed to be accurate at any time during the power pulse. Thus, while V_{CORR} is determined anecdotally to be largely accurate, there may be points during the power pulse where unexplained anomalies in the waveform may occur.

For this paper, the upstream location normally used to inductively correct the load voltage is Position G in Figure 1, so that V_{CORR} at G is labeled as V_{CORR}_G. Examples of current and voltage waveforms for an SMP diode shot (1540, discussed later in this paper) are shown (respectively) in Figs. 2a and 2b. The I_a and I_c currents at position G are shown in Fig. 2a, along with IBEAM for the shot. The currents at G are time-shifted forward (+6.75 ns) to facilitate waveform comparison with IBEAM. This is the same amount that the voltage at G (V_{MITL} in Eq. 3 above) is time-shifted to determine V_{CORR}. In Fig. 2b, the voltage at G is time-shifted forward

and compared to V_{CORR}_G. Also plotted is the inductive correction LdI/dt for the shot. It is seen that the biggest effect of the inductive correction is to decrease V_{CORR}_G with respect to the voltage at G early in the pulse. During the middle of the power pulse, V_{CORR}_G is decreased by ~ 0 – 0.5 MV compared to the voltage at G.

B. ITS modeling of the RITS SMP radiation field

A more schematic view of the SMP load region is shown in Fig. 3, including the dose and dose-rate radiation monitors deployed in the experimental test cell. At the upper left is the thin cathode stalk (typical diameter ~ 1 cm), and to its right the 1 mm-thick planar tantalum converter and aluminum beamstops. (The anode-cathode (A-K) gap is also shown within the red circle depicted in Fig. 1.) Also shown in Fig. 3 are four P-I-N diode dose-rate monitors positioned at various angles to the beam axis: (approximately) 0-degree direction (PIN_0), 45-degree direction (PIN_45), and 95-degree direction (PIN_95 and PIN_95 (uncoll)), where the label "uncoll' refers to an uncollimated detector. PIN_0 is collimated by a 3 cm-diameter aperture in a 7 cm-thick lead plate, located approximately midway between the converter and the PIN. The PIN_0 and PIN_95 (uncoll) monitors are located behind aluminum plates of 2.5 cm and 10 mm, respectively, but are otherwise unshielded. PIN_45 and PIN_95 are mounted inside tungsten collimators, limiting their fields of view to approximately 15 cm diameter at the converter position. PIN_95 (uncoll) was used to determine the effect of the collimator on the (collimated) PIN_95 detector. On a typical shot, the PIN_95 (uncoll) and PIN_95 detectors produced identical radiation waveshapes, but PIN_95 (uncoll) peaked at 1.8 – 2 times the value of PIN_95. This indicates that scattered photons in the RITS test cell increase x-ray measurements (PIN diodes and TLDs), which suggests a data analysis path that will be discussed further below.

Fig. 3 also shows the materials positioned in the field of view between the photon source and the P-I-N diodes. (In the case of PIN_45, the end flange of the vacuum, in its field of view, is eliminated for clarity.) Each P-I-N location is accompanied by thermoluminescent dosimeters

(TLDs) in close proximity. The ratio of TLD readings to the time-integrated P-I-N signal in each direction are checked after each shot, and found to have consistent values. Thus, the indicated dose-rate and dose indicated by the P-I-Ns tracks their respective TLD readings. In addition, the accompanying TLD readings can be used to give an absolute dose-rate for PINs 0 and 95 (uncoll), but not for PIN_95 and PIN_45. The latter is because while PIN_95 and PIN_45 are located within the tungsten collimators, the TLDs nearest to them are located outside the collimators.

The theory for comparison of predicted radiation from an intense electron beam from a diode such as the SMP with TLD readings is already well developed. Electron flow in the diode can be simulated in particle-in-cell (P-I-C) codes such as LSP[23]. The LSP output can then be used for input into the ITS code series, which converts electron flow into photon generation. Predicted dose output can then be compared to readings from TLDs deployed in the radiation space of interest. An alternative method foregoes the use of LSP, and instead posits electron trajectories onto the converter. In this method, electron flow is generally assumed to be from one of two categories: uniform-filled cone (UFC), i.e. electrons strike the anode with a range of angles between a minimum and maximum value; and 2) mono-angular, i.e. all electrons strike the converter at the same angle. The two assumptions yield two different dose predictions. Whether one or the other category is used can be decided depending upon which provides a better match to the time-integrated dose distribution. The TLDs however only give time-integrated information, so no conclusions can be reached about the evolution of the electron beam angle(s) with time. The UFC assumption is most relevant for comparison with time-integrated doses represented by TLDs, whereas mono-angular may be more appropriate to represent the time-dependent angles. The mono-angular assumption will be used for the CYLTRAN modeling described below.

We first illustrate a major motivation for the ITS-CYLTRAN modeling to be described shortly. In the analysis of any number of RITS shots in which the various dose-rates were intercompared, the dose-rates for the 0° and 95° directions appeared to change in opposite directions with respect to each other. An example of this is shown in Fig. 4. Waveshapes for the PIN_95 and PIN_0 detectors are shown for RITS Shot 1540 (current and voltage waveforms already shown

in Figs. 2a and 2b). The relative magnitudes of the two signals are quite different, and for this plot, the peaks are scaled in a heuristically useful way. With the scaling shown, the two waveform shapes are observed to track each other early in time, after which PIN_0 decreases rapidly. At the same time as PIN_0 decreases, PIN_95 increases just as strongly. At the same time, the calculated diode voltage for Shot 1540 is relatively constant during most of the radiation pulse. This behavior, dose-rate changing in opposite directions for the 0° and 95° directions, occurs quite frequently in the RITS SMP shot dataset. Recall that from the scaling of dose-rate indicated in Eq. 1, dose-rates are affected by the current, voltage, and electron angle. Since the current and voltage are the same for the PIN_0 and PIN_95 monitors, the fact that one monitor rises while the other falls at the same time implies that the x-factor behaves quite differently for the two different directions. This then can be considered the motivation for the ITS-CYLTRAN modeling to be undertaken below.

The following is a description for the time-dependent dose-rate analysis method developed in this paper:

The alternative method of posited electron beam behavior (mentioned above) is used. Electrons are simply assumed to strike the RITS-6 converter package at both specific angles: 0° – 80° in 10-degree increments, and specific energies: 1-10 MeV in 1 MeV increments. Here the 0° angle means parallel to the radiation axis, whereas the 80° angle is almost perpendicular to the axis. The ITS -CYLTRAN code (cylindrical symmetry) is then used to calculate photon spectra for each combination of electron angle and energy, for a total of 90 CYLTRAN calculations. Electrons that are backscattered from inside the tantalum anode are re-injected to mimic the effect of the diode electric field (also called “albedo suppression”). This artificial albedo suppression is required to ensure the electron’s energy is deposited in the converter package. It is assumed that the re-injection angle is unimportant since this angle will be randomized by the scattering events that result in the backscattering. This assumption will be checked in the future using PIC calculations relevant to RITS parameters. Photon spectra are extracted in the 0-10°, 40-50°, and 90-100° polar angle bins (angles correlated with the three PIN locations). Mass attenuation/absorption coefficients are used to attenuate the spectra as appropriate in each

direction and calculate the dose-rate in CaF_2 for each of the three PIN detectors. These 270 data points are then fit to dose-rate equations of the form:

$$D\_N(krad - cm^2/s/A) = c\_N \times V(MV)^{x\_N} \quad (4)$$

where the "c_N" and "x_N" parameters for each detector direction (N = 0°, 45°, 95°) are listed in Table 1. The fit assumes that the data follow a simple power-law for dose-rate as a function of electron energy for each electron angle. The accuracy of this assumption varies with individual angles and observation directions. Two examples of the fit quality are shown in Figs. 5a (best fit) and 5b (worst-case fit). These plots show the origin of the "c_N" and "x_N" terms listed in Table 1. A clear conclusion from Figs. 5a and 5b is that the use of IV^x scaling is a useful approximation to the dose-rate data, as opposed to a precise law of physics.

Eq. 4 then constitutes a "Radiographer's equation" that is specific to the RITS experiments. For this calculation, it is assumed that a constant percentage of the IBEAM current (15%) is composed of ion current, so IBEAM is multiplied by 0.85 to estimate the electron current. This is consistent with previous assumptions about the level of ion current on a typical RITS SMP shot[1].

In Eq. 4, the dose-rate is a measured quantity for a given shot. Since Table 1 gives both c and x terms for a given assumed electron angle, the equation can be solved for the diode voltage V. These voltages can be compared with the diode voltage waveform, yielding an estimate for electron angle at a given voltage at a given point in time. Since the number of voltage and angles used is limited, estimates are confined to 10-degree increments. A more detailed picture of angles and voltages could be constructed simply by increasing the number of CYLTRAN simulations.

Table 1 includes two c and x values for the 0° direction. RITS shots are divided into two large groups. In the earlier group, the 2.5 cm-thick aluminum mounted in front of PIN_0 was not present, having been put in position afterwards. Accordingly, for the earlier shots, fit parameters end with "a", while for the later shots, they end with "b." To better illustrate the scaling differences caused by the use of various thicknesses of attenuating material, the Table 1

parameters are depicted graphically in Figs. 6a (powers) and 6b (coefficients), both plotted as a function of electron angles. In Fig. 6a, the curves with and without the 2.5 cm-thick aluminum (x_0a and x_0b respectively) occur relatively close together, while in Fig. 6b, the coefficient curves are quite far apart. A brief study of material variation in the path to the 45° PIN (not plotted) shows similar behavior.

A scan of the predicted coefficients and powers for the three PIN detector directions in Table 1 is qualitatively instructive. In the 0° direction (axial), as the electron angle to the converter increases, the power and coefficient values decrease. This scaling has been already pointed out for HERMES electron beams[21,24]. For example, with the 3.1 cm filter in the 0° direction, if all the electrons strike the converter at 10°, the dose-rate scales as $IV^{2.68}$, and for a 30° strike angle, the dose-rate scales as $IV^{2.36}$. However, in the other two directions, the predicted scaling of the x-factor with angle does *not* scale as in the 0° direction. In the 95° direction (e.g. ~ normal to the radiation axis), the scaling is opposite that of the axial direction. As the electron angle increases from 10 to 80 degrees, the power *increases* from 1.69 to 1.94, with the coefficient also increasing. This is consistent with the qualitative behavior of the 95° PIN compared to the 0° PIN shown in Fig. 4. In between these two directions, the 45° parameter trends follow neither that of the axial nor the normal direction. There, the power increases slightly from 2.48 to 2.57, then decreases slightly to 2.36, with the coefficient following a similar trend. The maximum power parameter corresponds to the electron angle of incidence being in line with the detector angle of observation.

In the ideal case that the ITS data correspond to the PIN measurements, the ratios of the 45°/95° and 0°/45° signals would determine the time-dependent electron angle and voltage. In practice, the dose-rates at the off-axis PINs yielded predicted angles which were about twice the angle of those predicted for the forward direction. We chose the smaller angles implied from the 0°-direction for several reasons. One reason is that analysis of the PIN data from a shot series in which the A-K gap was systematically varied yielded an inferred electron angle which decreased steadily as the A-K gap was increased, consistent with what might be intuitively expected. More importantly, the smaller angles from the forward direction are more consistent with angle estimates resulting from prior research work with the SMP diode. If one assumes a 12.5 mm

cathode – 12 mm A-K gap SMP geometry with a ~few mm achieved spot size, and draws a straight line from the outer edge of the cathode to the edge of the anode spot, the line has an angle of ~ 24° to the axis. While this is certainly an oversimplified picture of the electron orbits in an SMP diode, it should pointed out in other SMP diode experiments, 30° is a common value assumed or concluded by previous researchers[18,22,25]. As far as the actual behavior of the electron orbits, LSP simulations including those at AWE[26,27] suggest complex trajectories for electrons emitted off the cathode annulus, with electrons spiraling into and around the beam axis before reaching the anode, and then impacting the anode. It is not clear what effective angles on the converter might be due to these orbits. However, earlier work at AWE[28] led to the conclusion that the electron angle at the converter of an SMP diode has a mean angle of approximately 27°. This is consistent with estimates of Hinshelwood et al[22,25] of electron angles (for a 1:1 aspect-ratio SMP diode) of between 20° and 30°.

Since the 0°-direction electron angle data from RITS appears to be consistent with the larger body of SMP diode experiments previously undertaken and cited above, the decision was made to emphasize the 0°-direction data as of primary importance. Then in order to make further analytical progress, two paths are possible:

1) assume that the 0°-direction data are quantitatively as well as qualitatively correct, and that the dose-rate data in the other two directions, combined with diode voltage data, can contribute important qualitative validation in a self-consistent picture of SMP diode dynamics;
2) make additional assumptions about the CYLTRAN data in the other angular directions which can enable a quantitative analysis of beam dynamics to be added to the 0°-direction data. We discuss the first path, and then the second path in the discussion below, and then show that the two analytical paths reach approximately the same conclusions.

One possible reason for the failure of the ITS-CYLTRAN data to fit the 45° and 95° PIN data is due to an indicated abundance of scattered photons in the RITS experimental cell, which affect the interpretation of the CYLTRAN data. A key observation that illustrates this is that a comparison of the dose-rate measured by the respective PIN_95 and PIN_95 (uncoll) monitors

shows that while the waveshapes are almost identical, the uncollimated monitor gives twice the amount of signal as the uncollimated one. Since neither of the TLD sets associated with the 95° direction (see Fig. 4) are collimated as well as the collimated PIN_95 detector, it is apparent that the TLDs in the 95° direction are exposed to both direct and scattered photons. This makes the dose that they measure higher than those predicted by the CYTRAN modeling. In contrast, the axial field of view towards PIN_0 and TLDs 1-4 (Fig. 2) is collimated by a small (3 cm-diameter) aperture in an otherwise large lead shield located approximately midway between the diode and PIN_0, followed by a 2.5 cm-thick aluminum plate (in the later set of RITS shots) placed directly in front of the PIN. Evidently, this level of shielding from scattered photons is more successful compared to the other two directions. In retrospect, for this experiment (and for any future experiments), one way to address the scattered photon possibility would be to install specially designed TLDs within the tungsten collimator in which PIN_95 is mounted. Given that this was not done here, the question is whether additional assumptions about the 95° dataset can be made to reconcile the data with that in the 0°-direction. That will be the subject of the second path listed above and pursued below.

Despite the fact that the ITS modeling appeared to yield quantitatively correct predictions for only one out of the three observation directions, the three datasets can be combined to yield consistent *qualitative* data about the electron beam angles. This idea will be further developed below. Anecdotal evidence provided by analysis of significant numbers of RITS shots indicates that the *trend* in the x-factors in Table 1 appears to be accurate. That is, the x-factor for the 45° PIN direction appears to scale in a mixed way by inferred changes in electron direction, while that for the 95° PIN does appear to increase as the electron angle increases. Then while the PIN data in the 0° direction can be used to infer an electron angle that is roughly correct quantitatively, the 95° data from PINS_95 and/or 95 (uncoll) can be used as a self-consistency check on the 0° direction. So, for example, if the 0° detector analysis points to an increase of the electron angle with time (PIN_0 declines with time), the 95° P-I-N magnitude should be *rising* at the same time, and the 45° P-I-N should behave somewhere in between the other two. If, on the other hand, both PIN_0 and PIN_95 decrease in magnitude when compared with the respective scaled IV^x waveforms, this does not point to an angle change, but instead suggests that the corrected voltage waveform may not be correct at some point in the power pulse. As stated

previously, the method of correcting the MITL voltage to the diode location (Eq. 3), while approximately correct, contains some assumptions about the current and voltage coming forward that may not be correct at each point in time.

III. Examples of self-consistent estimates of electron angle change with time using 0°-direction data quantitatively, and 95°-direction qualitatively.

This is the first path of analysis mentioned above. As an illustration of this analysis procedure, consider SMP shot 1780, a shot taken with an 8.5 cm-diameter cathode and an 8.3 cm A-K gap, a configuration known as '8.5 – 8.3'. This shot is chosen for discussion because it belongs to a subset of RITS SMP shots in which the inferred electron angle appears to remain constant, even though the radiation pulse terminated early, due to some kind of impedance collapse. (One interpretation of this behavior is that the short full width at half maximum (FWHM) precluded any development of beam angle changes that would occur on a full-pulse shot.) The shot featured a bare tantalum target (whereas normally the tantalum is located behind a thin aluminum foil), a non-standard anode configuration that may have contributed to the early impedance collapse. The radiation pulse FWHM was only 19 ns instead of the more typical ~ 45 ns. Initial estimates of corrected diode voltage using MITL voltages calculated at both F and G positions (V_{CORR}_F and V_{CORR}_G) are plotted with the (scaled) axial PIN_0 signal in Fig. 7a. Note that a) both estimated load voltages are almost identical, indicating that the estimated forward-going voltage remains relatively unchanged from Position F (out of view in Fig. 1) to Position G; and b) the corrected voltage waveforms *increase* after the point where the radiation pulse decreases quickly. This is a typical corrected voltage behavior for RITS shots with premature impedance collapse, and where the Eq. 3 calculation leads to an incorrect waveform, since the radiation pulse is clearly collapsing at that point. The source of the incorrect calculation is most likely the strong retrapping wave that is generated when the load impedance collapses, which violates the equilibrium flow assumption underlying the Mendel voltage calculation (Eq. 2).

Using Eq. 4 and Table 1, three estimates of diode voltage are calculated from the (axial) PIN_0 dose-rate using assumptions of 20°, 30°, and 40° electron angle, respectively. The dose-rate is

calculated by scaling the PIN signal so its time-integral is equal to the dose. These estimates are plotted against the V_{CORR}_G waveform (shown in Fig. 7a) in Fig. 7b. In this plot, there are no adjustable parameters, e.g. the three voltage estimates are directly calculated from Eq. 4. As can be seen, apart from increased noise at low voltage, the inferred voltage matches V_{CORR}_G quite well for the 30° electron angle, up to the point where the unfold voltage derived from PIN_0 decreases. The three different PIN waveforms for the different detector directions are plotted (normalized to 1) in Fig. 8. Their shapes are quite similar up to the point where PIN_0 collapses. After that point, the PIN_0 magnitude falls the most severely, and PIN_95 falls the least amount. The drop in PIN_45 falls somewhere in the middle. All three show a late-time peak.

A modification to V_{CORR}_G is now constructed which consists of the following: the rising part of the original V_{CORR}_G waveform is retained. After the point at which PIN_0 collapses, the late-time piece of the voltage unfold for the 30° electron angle assumption is combined with the rising part of V_{CORR}_G. The resulting 2-piece waveform is shown in Fig. 9, where the peak corrected voltage reaches approximately 6 MV. The modified V_{CORR}_G can be qualitatively compared to the normalized dose-rates for the three PINs plotted in Fig. 8. Given that the set of x-factors for the 95°-direction are less than those in the 0°-direction, the tendency of PIN_0 to fall faster than PIN_95 after the peak simply reflects the higher power-law scaling in that direction. The behavior of the 45° PIN is less well understood, given that the x-factor in the 30° direction (and any greater angle) predicted by CYLTRAN is in fact greater than for the angles in the 0°-direction. One feature in the Fig. 8 waveforms is a slight dip in magnitude that occurs just before all three reach their peak. Since the dip occurs in all three plots, and the dip does not occur in the corrected voltage (Fig. 7b), we conclude that the calculated V_{CORR}_G waveform is incorrect in this part of the curve fit, in that the voltage estimate from Eq. 3 is too high. That discrepancy could be addressed separately. Otherwise, this exercise leads to a construction of the diode voltage that is at least qualitatively consistent with two of the three PIN signals, PIN_0 and PIN_95, with the inferred electron angle remaining roughly constant at 30° during the radiation pulse. That the angle could remain constant even as the diode impedance is clearly observed to collapse is quite notable.

The utility of the use of the three different PINs at different angles is rendered more valuable when, unlike Shot 1780 above, the inferred electron beam pinch angle is *not* constant. A survey of shot types in the RITS database indicates that the inferred pinch angle behavior divides into several distinct types: a) an angle varying within a range in time, indicating a relatively stable pinch, b) pinch angle increasing with time, as often happens with 8.5 – 8.3 shots, and c) pinch angle changing in both directions, e.g. increasing then decreasing with time. The latter behavior can be interpreted as some kind of oscillation in the beam pinch angle. We present examples of all three types of behavior below, using the same methodology as described in the Shot 1780 example.

As an example of type a) behavior, we discuss a category of RITS SMP shots which exhibited stable and reproducible behavior. These shots featured a 12.5 cm-diameter cathode and 12 mm A-K gap ('12.5 – 12'). One of these, Shot 1908, exhibited a full (47 ns) pulse-width and the highest recorded dose of any SMP shot. A plot of the (scaled) PIN waveforms (similar to Fig. 8 for Shot 1780) is shown in Fig. 10a. The PIN behavior here is different from Fig. 8, in that (with the scaling used here) while the PIN_45 and PIN_95 waveshapes are almost identical, the PIN_0 signal early in time shows a relatively decreased dose-rate compared to the other two. It then rises during the pulse, and reaches a late peak, even as the other two dose-rates have begun to fall. And, as in Fig. 7b for Shot 1780, three estimates of diode voltage calculated from the PIN_0 dose-rate using Eq. 4 and Table 1 (20°, 30°, and 40° angle assumptions) are plotted with the V_{CORR_G} waveform for Shot 1908 in Fig. 10b. Here, as contrasted with Fig. 7b, the apparent angle behavior appears more complex than in Shot 1780, where (at least before the impedance collapse), the 30° angle matched the V_{CORR_G} waveform fairly well. On the initial rise, the V_{CORR_G} waveform for Shot 1908 appears to contact the 20° angle assumption curve, and then again just prior to the end of the radiation pulse. In between, the corrected voltage appears to vary around the 30° curve, and reaches as high as 40°, before returning to 20° late in the pulse. This behavior could be due to either a) the electron angle changing as indicated, or b) the corrected voltage waveform being somehow not accurate. A further discussion of this shot below will conclude that a) is the correct interpretation.

As an example of type b) behavior, we consider Shot 1540, whose current and voltage waveforms were shown in Figs. 2a and 2b. This shot was from a series of shots at the 4.5 MV output level, and featured a cathode of 7 mm diameter with a 6 mm A-K gap ('7-6'). This shot was chosen for discussion here, because the axial PIN_0 signal exhibited a peak early in the pulse, followed by a steady decline in dose-rate for the remainder of the power pulse. Since the FWHM for the shot was 40 ns, a premature impedance collapse is not suspected, yet the cause of the considerable drop-off in dose-rate would be useful to understand. A plot of the PIN_0 waveform for Shot 1540 is shown in Fig. 11. One possible cause for the PIN_0 decrease is a decrease in load voltage, if not an outright collapse. Yet the estimated diode voltage for the shot (V_{CORR}_G), also shown (scaled) in Fig. 11, does not indicate such a voltage decline, although there are ± 10% oscillations near the peak voltage that may have related signatures in the PIN dose-rates. A further clue is given by comparing the 0° and 95° PIN signals (PIN_0 vs PIN_95). A (scaled) plot comparison is shown in Fig. 4. Unlike the axial dose-rate, the 95° signal *rises* just as the former falls. The prior discussion then points to a possible change in the electron beam angle during the pulse.

As a test of the angle-change hypothesis, we plot the V_{CORR}_G waveform (shown in Fig. 10) against the voltage estimates derived using Eq. 4 for the axial dose-rate. That is, the equation is solved for V using the PIN_0 dose-rate for four different electron angles: 10°, 20°, 30°, and 40°. The derived voltages are then plotted against the estimated voltage curves. The plot comparisons are divided into early-time (Fig. 12a) and late-time (Fig. 12b), simply for clarity. (Various segments of V_{CORR}_G are colored differently to facilitate comparison.) The first observation is that the V-curves steadily increase as the presumed electron angle increases. The second observation is that, as in the Shot 1780 case, the various pieces of V_{CORR}_G appear to follow each of the V-curves at some point. For example, the first section of V_{CORR}_G tracks between the 10° and 20° curves. The second section tracks the 30° curve very closely. The third section rises to the 40° V-curve. In Fig. 11b, the fourth section returns to the 30° curve. The last two V_{CORR}_G pieces oscillate up and down, but can be correlated roughly with the 40° curve. At the end of the power pulse, the V_{CORR}_G waveform follows the 40° curve precisely, because that portion of the corrected voltage is set to the 40° curve, just like with the example above.

The correlation here between the V_{CORR}_G waveform and the various V-curves is not precise, because the angle cuts are set at 10° apart. Again, one could imagine a more detailed model based upon more angle cuts, but the procedure discussed here, however crude, illustrates the principle. With the current model, one clear interpretation of the V_{CORR}_G - V-curve comparison is that as the power pulse evolves, the electron angle increases steadily, starting out in the 10-20° range, and ending at 40°. It is this increase in the angle with respect to the radiation axis that results in the dose-rate decrease in the forward direction, even as the indicated diode voltage remains somewhat constant. This shot is one of many that upon similar examination exhibit such a drop in dose-rate as the power pulse evolves. The common factor connecting such shots is that the diode aspect ratio is less than 1:1, that is, the A-K gap is less than the cathode diameter. This results in reduced diode impedance, and evidently leads to the tendency of the electron beam to pinch inward on itself during the power pulse. One possible explanation for this is the observation that it in a number of SMP experiments at different facilities[28], the most successful operation occurs with diode with 1:1 aspect ratio, e.g. the cathode diameter is equal to the A-K gap. Given that such as intense beam propagates with both electric and magnetic fields present, a 1:1 aspect ratio may represent the most stable balance between the two forces. If then the A-K gap is reduced, the diode current increases, and now the beam self-magnetic field may begin to dominate the electric field, leading to the observed inward-pinch behavior.

There is a check on this inference of increased electron angle as the radiation pulse evolves, which requires some explanation. As already mentioned, the x-factors for the off-axis PIN_95 and on-axis PIN_0 monitors change in opposite directions as the electron pinch angle changes. The two monitors can be coupled mathematically in a heuristically useful manner. The PIN_0 waveform is divided by the PIN_95 waveform (with appropriate time-shifts to take propagation time to each monitor into account), and the result is normalized to unity. The resulting waveform is referred to as PIN_0/PIN_95. When this waveform peaks, it is an indication that the pinch angle is the smallest, and when it falls, the angle is then increasing. This inferred behavior is qualitative, not quantitative, since only the PIN_0 signal behavior has been characterized completely by CYLTRAN modeling. The (scaled) PIN_0/PIN_95 waveform is plotted against the composite IV^x waveform in Fig. 13. To construct the composite IV^x waveform, each of the six V_{CORR}_G pieces is scaled with the x-factor and coefficient associated with the various

electron angles. The PIN_0/PIN_95 signal is observed to decrease in time at a rate that roughly coincides with the drop in the composite IV^x waveform. This provides more anecdotal evidence for the validity of the electron beam angle increasing with time.

To illustrate the type c) behavior mentioned above, e.g. pinch angle changing in both directions during a pulse, only one plot is presented which is shown as an anecdotal example of this behavior. The three (scaled) PINs for Shot 1850 are plotted in Fig. 14. The waveform plot is limited to the main part of the radiation pulse for clarity, and the waveforms, as usual, have been timeshifted to reflect radiation transit time to each PIN. This shot featured an unusual geometry compared to the other shots discussed so far, in that the MITL cone was removed (see Fig. 1). The cathode diameter was 12.5 mm, and the A-K gap was 12 mm ('12.5 – 12'). Perhaps because the MITL cone was removed, the shot was characterized by asymmetric current flow in azimuth at the IBEAM location. In Fig. 13, the three PINs are observed to rise to the first peak together, and then undergo a series of oscillations in which the relative peaks in PIN_95 and PIN_0 switch places, that is, first PIN_0 exceeds PIN_95, then PIN_95 exceeds PIN_0, and so on. This happens a total of six times. For the first 5 of the 6 times, the PIN_45 waveform is observed to track along with PIN_95 and counter-cyclical to PIN_0. Then for the sixth time, PIN_45 is observed to switch from tracking PIN_95 to tracking PIN_0 as both PIN_0 and PIN_45 decline relative to PIN_95. The behavior of these counter-cyclical swings cannot be ascribed to timing errors, and provides anecdotal evidence for some kind of oscillation in the electron pinch angle. If such oscillations did occur, this did not affect the radiation pulse FWHM, which was 50 ns and thus was clearly a full-pulse shot.

IV. Self-consistent estimates of electron angle change with time using quantitative estimates of both 0°-direction and 95°-direction data.

This is the second path of analysis mentioned above. In this case, since only the 0°-direction data appears yield appropriate electron angles, we have to make some assumption about the 95°-PIN dataset in order to proceed further. We have previously stated that the TLDs in the 95°-direction appear to be exposed to both direct and scattered photons, and as evidence, the dose-rate measured by PIN-95 (uncoll), while almost identical in waveshape to the PIN_95 monitor, is

twice the size as that of PIN_95 on almost all RITS SMP shots. Thus, it appears logical to assume that the TLDs associated with the 95° PINs (see Fig. 3) accumulate twice the dose that they would in the absence of scattered photons. As a result, we make the following analytical assumption: all the TLD data in the 95°-direction are to be reduced by a factor 2 in order to compare with CYLTRAN calculations. We state this as an assumption, and then show in the subsequent discussion below that the results are self-consistent with both diode voltage data, and with the conclusions of the first path above.

With the factor-2 reduction in the 95°-dose rate assumed above, we can compare CYLTRAN results with the absolute dose-rates in both the 0°- and 95°-directions. One way to do this is by forming a two-dimensional plot, where the 0° dose-rate is plotted on the x-axis, and the 95° dose-rate on the y-axis. The units are chosen to match the left-hand side of Eq. 4 (krad-cm^2/s/A), where the absolute dose-rates are divided by (85% of) the diode current IBEAM. The CYLTRAN outputs are plotted in the form of two contour plots: 1) constant voltage (1 to 8 MV) with electron angle varied, and 2) constant electron angle (0 – 80°) with voltage varied. The resulting contour plots are shown (respectively) in Figs. 15a-b. Note that: a) these are plots of CYLTRAN output only, do not include any corrected voltage data, and are not specific to any particular RITS shot; and b) since the RITS dataset includes shots taken with and without the 2.5-cm aluminum plate in front of PIN_0 (Fig. 3), there are in fact two sets of contour plots used as appropriate for a given shot.

To these two contour plots, we then add absolute dose-rate information for a given shot, again with the assumption that the measured dose-rates for the 95°-direction must be reduced by half. The first example of the two composite plots (voltage and angle) are for the first shot discussed in Section III above, Shot 1780. On this shot, the radiation pulse FWHM was reduced to 19 ns, and the conclusion from the qualitative analysis is that the dose-rate data are consistent with a constant electron angle on the converter of 30°. The composite plots for Shot 1780 are shown in Figs. 16a (voltage contours) and 16b (angle contours). The black and red dots in the plots are data points at each time step, with black dots tracing the progress in time up to the peak dose-rate in the 0°-direction, and red dots are for times after this peak. Besides the voltage and angle data, the 3-digit numbers shown next to the red-black curves in Fig. 16a refer to the time shown in the

data plots for Shot 1780 in Figs. 7-9. The data points progress approximately from the southwest to northeast, then return to southwest again. While the individual data points are somewhat scattered, the plot with the voltage contours (Fig. 16a) indicates an approximately steady increase to a peak voltage of 6.4 MV, while the plot with the angle contours (Fig. 15b) points to an electron beam angle of between 30° and 40°, with an angle at peak 0°-dose-rate of 30°. While the indicated angle is consistent with the prior qualitative discussion, the composite plot in voltage provides a self-consistency check on the assumption of reducing the 95° dose-rate by factor 2. The indicated peak voltage attained by Shot 1780 in Fig. 16a is approximately 6.4 MV. This compares to a V_{CORR}_G peak value of 6.0 MV, a 6.7% discrepancy. Given that the factor 2 is only a rough approximation, this affirms that the assumption of half-the-dose-rate for the 95°-direction is approximately correct. Viewed another way, if the full dose-rate were used in the 95°-direction, the plotted curve would extend to beyond the range of CLYTRAN values shown in Fig. 15a, which is inconsistent with what multiple analyses of RITS shots (including the V_{CORR}_G calculation) have determined[29].

We make some observations (and caveats) about the data plots in Figs. 16a-b. Part of the fluctuations seen in the plots are due to a base level of noise in the RITS data acquisition system. This noise level contributes an increased level of fluctuation when the signal level is low. Accordingly, the most important section of the data plot is when the signal level(s) exceed ~ 20% of the peak levels seen, e,g, towards the middle section of the radiation pulse. For instance, a large excursion in the plots in both Figures occur near the 3 MV voltage contour (early in the pulse). This reflects a sharp and short-lived dip in the PIN_0 signal early on the signal rise, a feature not recorded on the PIN_95 signal. It is not clear whether this dip is real, or a signal artifact. Referring to Fig. 1, early in the SMP shot power flow, MITL flow current is diverted[1] by the field shaper to the outer 'dustbin' wall before being magnetically pulled back towards the load region by the rising cathode current. During this phase, x-rays generated by the electron strikes to the outer wall can be observed by PIN_95, and especially by PIN_45, but not by PIN_0. Since this loss current does not contribute to the useful radiographic pulse, it could be ignored in the angle analysis. In Fig. 8, an enhanced level of dose-rate is captured by PIN_45, but not seen on the other two PINs, and is likely due to the MITL flow loss.

Another source of x-ray radiation observed by PIN_95, but not by PIN_0, occurs and is often correlated with a shortened FWHM caused by a diode impedance collapse. Apparently, some fraction of the MITL flow current not captured in the cathode current is diverted to and impacts the side of the cylinder in which the tantalum converter is mounted. The radiation so generated is observed by PIN_95, but not by PIN_0. This does not appear to be the case in Shot 1780 (Fig 8), since a late-time spike in the dose-rate occurs for all three detectors. This spike is the source of the loop-shaped feature in both Figs. 16a and b, lying between the 4 MV and 5 MV contours at about 2.33 μs. The beam thus appears to increase its angle from 40° to 60° for a time, and then returns back to 40°. On any number of other RITS shots, however, a late-time spike in PIN_95 is not matched by a similar spike in PIN_0. The cause in these cases appears to be a side-strike to the anode cylinder, and sometime correlated with an off-center bright spot in the x-ray pinhole camera image that observes the diode region. With such a side-strike, the CYTRAN analysis cannot (and should not be expected to) explain the presence of a spike in PIN_95 and not in PIN_0.

A positive feature of such composite data plots as Figs. 16a-b is that voltage and angular information can be gleaned for any time during the power pulse for which dose-rate data exist. This is contrast to the inference of electron angle determined by plotting V_{CORR}_G against the invert curves using Eq. 4 for the various electron angles (see Figs. 7a and 7b). This is because the CYTRAN modeling is only performed for discrete angles. A less-desirable aspect of the composite data plots is illustrated by referring again to Fig. 7b, which illustrates the advantages of a visual data presentation (with time as the independent variable) as compared to the composite data plots. In the Figure, a visual waveform comparison of the diode voltage before peak, compares quite well with the voltage invert using Table 1 and Eq. 4 for a 30° assumption, with two exceptions: a sharp but short-lived drop in the PIN_0 invert on the waveform rise, and a decrease in the PIN_0 invert near peak power, are indicated visually as a small deviation in the waveform comparison. The sharp dip on the rise is not repeated in the other two PINs (see Fig. 8), but the decrease near peak power occurs on all three PINs. The latter is ascribed in Section III as due to a faulty diode voltage calculation at this time. The first dip may be real, or an unknown artifact of the PIN_0 recorded waveform. In either case, one might consider these as minor deviations in the general narrative of approximately constant electron beam angle. In the

composite data plots, the same points in time appear as large excursions in the plots which may appear to some as overemphasizing the deviations.

The second example of the utility of composite plots is that of the second shot discussed in Section III, Shot 1908, one of the series of configuration 12.5 – 12 SMP shots that demonstrated relatively stable and full-power radiation behavior. In Section III, the inference from comparing the V_{CORR}_G and voltages deriving from the assumed electron angles was that the pinch angle started and ended at 20°, but varied between 20 and 40° in between. The composite plot of the angular behavior of Shot 1908 (analogous to that of Shot 1780 in Fig. 16b) is shown in Fig. 17. In this plot, the black dots trace the progress of the radiation pulse up to the first peak in the inverted PIN_0 waveform (see Fig. 10b), the red dots trace the radiation pulse after the second peak in the inverted PIN_0 waveform, and the yellow dots cover the time in between the two peaks. It is observed that the last of the black points (e.g. just before the first peak) and first of the red points (e.g. just after the second peak) are both located near the right-most plot of data points on the Figure, and nearly exactly on the 20° angle curve. In between (yellow points), the pinch angle traces out a complex trajectory of angles between 20° and ~ 35°. Both these observations are completely consistent with the inferred angle behavior in the previous analysis of Shot 1908 in Section III.

A third example of composite waveform plots is that of Shot 1540, already discussed in Section III above. The conclusion from the qualitative analysis is that the electron beam angle began early in the pulse at ~ 10-20°, and ended at approximately 40°, having evolved towards larger angles during the radiation pulse. Plots analogous to Figs. 16a-b (for Shot 1780) are shown in Figs. 18a-b. In Fig. 18b, the angle traced out by the black (prior to peak D_0) curve decreases from ~ 40° to 25° at peak power. In the later part of the radiation pulse (red), the plot traces out a rather complex path in the which the angle increases to 50°, then doubles back on itself before evolving to a ~ constant 60° late in the radiation pulse. While the minimum and maximum beam angles are each ~ 10° greater than those inferred from the qualitative analysis, the trend towards increasing angle is consistent with the earlier analysis. In Fig. 18a, the estimated diode voltage peaks at ~ 4.6 MV, consistent with the 4.75 MV peak for V_{CORR}_G for the shot. Comparing Figs. 18 with Figs. 16, one can say that, very qualitatively speaking, if the southwest-to-northeast

excursion in the dose-rate data extends narrowly in width, the beam angle change is relatively small, whereas if the excursion width is larger, the beam angle change is greater during the radiation pulse.

One final example of composite data plots is included here, and for a shot that was not discussed in Section III. Shot 1774 was taken at full power (8 MV), and featured a standard foil-over-tantalum anode in which the radiation pulse was terminated prematurely (FHWM = 21 ns), evidently by an impedance collapse. Prior to the radiation pulse termination, however, the forward dose-rate (PIN_0) peaked at the highest amount recorded for any RITS SMP diode shot. This shot is included in the discussion here for two reasons: a) the combination of very high peak dose-rate and premature impedance collapse seems somewhat anomalous, and worthy of investigation as to why; and b) the dose-rate peak for PIN_0 is reached well before the peaks in the other two PINs (PIN_45 and PIN_95), and also well before the inferred impedance collapse begins to occur.

Dose-rate behavior of the three PINs (0°, 45°, 95°) is plotted in Fig. 19, and scaled in a way that emphasizes the similar shape of the PINs prior to the dose-rate peak. Also plotted is the IBEAM current scaled so that the waveshape fits with the other signals. Here it can be seen that a) PIN_0 reaches its maximum in a rather narrow peak, and the same time that b) PIN_95 is observed to reach a local minimum, and c) PIN_45 magnitude lies somewhere in between the other two. This then has all the hallmarks of a change in beam pinch angle. Note that the slope in the diode current IBEAM reaches an inflection point, then rises suddenly as the PIN dose-rates fall sharply. Note also, however, that the PIN_0 falls first after it peaks, followed by PIN_45 and then PIN_95, which reaches its peak last. The total time interval between the beginning of the PIN_0 peak and the end of the PIN_95 peak is almost 10 ns. It is only when PIN_95 begins its fall that IBEAM undergoes an inflection point towards a much steeper current rise.

The composite data plots (voltage and angle) for Shot 1774 are shown in Figs. 20a and 20b, respectively. The shot takes a complex path in D_0 – D_95 space, where the beginning and end of the data occur at ~ 40° beam angle. In between, the angle approaches 20° on two occasions, during the rise and then, more significantly, at peak D_0. This clearly suggests that the

explanation for the high dose-rate observed in the forward direction is a fairly sudden decrease in the beam angle, and therefore IV^x is more peaked in the forward direction. Since the radiation dose-rate collapses very soon after this point, one may infer an oscillation in the beam angle which could have contributed to the radiation pulse termination. As a self-consistency check, the composite data plot in Fig. 20a indicates a peak voltage of ~ 8.3 MV, whereas the corrected diode voltage V_{CORR}_G has a 7.8 MV maximum, a discrepancy of 6%, in line with the shots previously discussed.

There is a way to display the data in the composite data plots that has the visual appeal of the data plots with time as the independent variable (e.g. Figs. 7-14 and 19). Referring to Figs. 15a and 15b, the points reflect the discrete voltage and angle values that served as the inputs for the CYLTRAN simulations. The individual data points in the composite plots (e.g. Figs. 16a and 16b), however, can be paired with more precise values of both voltage (15a) and angle (15b) by the use of mathematical interpolation. Then since each data point is associated with a value in time, the result is a depiction of both voltage and angle in time for a given shot. This is shown for Shot 1540 (Figs. 18a and 18b) in Figs. 21a and 21b. In Fig. 21a, the voltage estimate from CYTRAN interpolation is compared with V_{CORR}_G for the shot. The waveshapes match very well, but this is not what is most notable about this plot. The V_{CORR}_G data is obtained from Bdots measuring the upstream IVA bound and total currents, with the load voltage estimated using Eq. 2. The CYLTRAN interpolation data are strictly a result of the dose-rate measurements from the PIN_0 and PIN_95 monitors (and with the 50% reduction in PIN_95 TLD dose assumption, and 0.85 IBEAM). The two curves are thus derived from completely different sources. The plot of electron angle vs time in Fig. 21b reflects the previous conclusions (from Section III and earlier in this section) that after reaching a minimum of electron angle (~ 25°) when the voltage first peaks, the angle increases continuously through the rest of the radiation pulse.

And finally, a similar graphical display to that of Shot 1540 (Figs. 21a-b) is shown for Shot 1774 in Figs. 22a (voltage) and 22b (angle). In this case, the voltage estimated from CLYTRAN interpolation appears larger in places compared to the V_{CORR}_G waveform, suggesting that the factor-2 decrease in the 95° TLDs may not be as accurate as in the other shot. The time-

dependent angle, as compared to Shot 1540 (Fig. 21b), oscillates between a relatively narrow band of angles, as opposed to continuously increasing angular behavior, with decreases to as low as ~ 18° at peak power, the latter correlated with the very high peak in the 0° dose-rate seen in Fig. 19.

V. SUMMARY AND CONCLUSIONS

We have presented here a methodology for inferring the time evolution of the angle at which an intense electron beam strikes a bremsstrahlung converter. This represents an advance over previous angle determinations using an inverted form of a Radiographer's Equation to match time-integrated dose (TLD) measurements. The present method involves use of the CYLTRAN two-dimensional Monte-Carlo electron-photon transport code, plus experimental measurements of dose-rates from an array of monitors located at different angles with respect to the beam axis. In particular, our approach relies on the key determination from CYLTRAN calculations that predicts opposite scaling of the x-factor, as a function of time, for the forward (0°) radiation direction as compared to the 95° direction used for the RITS geometry. In this case, dose-rate information is provided by P-I-N diodes and TLDs, but other dose-rate diagnostics could also be used. In the ideal case, the CYLTRAN calculations could be used to infer the electron energy and angle as functions of time. In practice, in the case of the RITS data, only the forward (0°) data from CYLTRAN appeared to yield angular results consistent with results of both prior research efforts and other RITS diagnostics measurements. By halving the dose measured in the 95° direction to make it consistent with CYLTRAN and voltage measurements, a procedure is shown to calculate voltage and electron angle as functions of time, independent of upstream electrical measurements. Measuring the dose behind suitable collimation would remove the need for this adjustment and provide an independent way to determine the beam energy and angle of incidence with time resolution. Nonetheless, it is shown that combining the dose-rate information with estimates of diode voltage can lead to qualitative and even somewhat quantitative estimates of the evolution of the electron pinch angle with time. The methods shown in our analysis should

be applicable to many other pulsed x-ray sources where dose-rate measurements can be made at different polar angles.

ACKNOWLEDGEMENTS

Sandia National Laboratories is a multimission laboratory managed and operated by National Technology and Engineering Solutions of Sandia, LLC, a wholly owned subsidiary of Honeywell International, Inc., for the U.S. Department of Energy's National Nuclear Security Administration under contract DE-NA0003525.

Table 1. Power-law fit parameters x_N and c_N for the three PIN directions, dose-rate measurements for RITS data.

Filters:	0.6 cm Al		3.1 cm Al		5.85 cm Al		1 cm polycarb. + 1 cm Al	
e-angle	x_0a	c_0a	x_0b	c_0b	x_45	c_45	x_95	c_95
0	2.65	9404	2.80	5037	2.48	1670	1.69	2878
10	2.54	9266	2.68	4962	2.48	1686	1.71	2836
20	2.36	8500	2.50	4537	2.51	1680	1.72	2893
30	2.24	8001	2.36	4289	2.56	1664	1.74	2942
40	2.15	7398	2.28	3900	2.57	1636	1.77	3030
50	2.10	6952	2.21	3674	2.52	1578	1.81	3146
60	2.04	6831	2.16	3562	2.44	1547	1.86	3223
70	2.02	6528	2.14	3402	2.39	1515	1.93	3291
80	2.01	6342	2.13	3307	2.36	1492	1.94	4339

Bibliography

1. K. D. Hahn *et al*, IEEE Trans. Plasma Sci. **38** 2652 (2010).
2. M. S. Di Capua and D. G. Pellinen, J. Appl. Phys. **50** 3713 (1979).
3. J.M. Creedon, J. Appl. Phys. **46** 2946 (1975).
4. C.W. Mendel, D.B. Seidel, and S.A. Slutz, Phys. Fluids **26**, 3628 (1983).
5. C.W. Mendel, D.B. Seidel, and S.E. Rosenthal, Laser Part. Beams **1**, 311 (1983).
6. P.F. Ottinger and J.W. Schumer, Phys. Plasmas **13**, 063109 (2006).
7. P. F. Ottinger, T. J. Renk, and J. W. Schumer, Phys. Plasmas **26** 023105 (2019).
8. J. Maenchen, H. T. Sheldon, G. D. Rondeau, J. B. Greenly, and D. A. Hammer Rev. Sci. Instrum. **55** 1931 (1984).
9. Anne-Sophie T. Leclere, An Evaluation of Bremsstrahlung Cross-sections for keV to GeV Electrons, Thesis, Master of Science, University of Florida, 2001.
10. R. D. Evans, *The Atomic Nucleus*, McGraw-Hill, 1955.
11. H. W. Koch and J. W. Motz, Rev. Mod. Phys **31** 920 (1959).
12. S. M. Seltzer and M. J. Berger, Nucl. Instr. Meth. Phys. **B12** 95 (1985).
13. S. M. Seltzer, Int'l Journal of Radiation Applications and Instr. **A42** 917 (1991).
14. B. C. Franke, R. P. Kensek, T.W. Laub, and M. J. Crawford, *ITS Version 6: The Integrated TIGER Series of Coupled Electron/Photon Monte Carlo Transport Codes, Revision 5*, Tech. Rep. SAND2008-3331, Sandia National Laboratories (2013), (unpublished).
15. J. F. Briesmeister, *MCNP – A general Monte Carlo N-particle transport code, Version 4C*, Los Alamos National Laboratory, Los Alamos, NM, LA-13709-M, Mar. 2000 (unpublished).
16. W. W. Buechner, R. J. Van de Graaff, E. A. Burrill, and A. Sperduto, Phys. Rev. **74** (1948), 1948.
17. W. Heitler, *Quantum Theory of Radiation* (University Press, Oxford, England, 1936).
18. I. Crotch, *Radiographer's equations for megavolt electron beams*, IEEE Conference on Plasma Science (ICOPS 2004), p. 183.
19. J.J. Ramirez, K.R. Prestwich, J.A. Alexander, J.P. Corley, D.G. Denison, C.W. Huddle, D.L. Johnson, T.W.L. Sanford, I.O. Seamons, G.A. Zawadzkas, I.D. Smith, P.W. Spence,

and L.G. Schlitt, in the *Proceedings of the 7th International Conference on High Power Particle Beams*, Karlsruhe, Germany, 1988 edited by W. Bauer and W. Schmidt (Kernforschungszentrum, Karlsruhe GmbH, Karlsruhe, Germany, 1988), p. 148.

20. J. A. Halbleib and T. W. L. Sanford, Sandia Report SAND83-2572, September 1985 (unpublished).
21. T. W. L. Sanford, Sandia Report SAND2013-2481, Sandia National Laboratories, April 2013 (unpublished).
22. D. Hinshelwood, R. Allen, R. Commisso, G. Cooperstein, B. Huhman, D. Mosher, D. Murphy, P.F. Ottinger, J. Schumer, S. Swanekamp, S. Stephanakis, B. Weber, F. Young, I. Crotch, J. O'Malley, and J. Threadgold, IEEE Trans. Plasma Sci. **35** 565 (2007).
23. LSP is a software product of ATK Mission Research, Albuquerque, NM.
24. T. W. L. Sanford, J. A. Halbleib, J. W. Poukey, C. E. Heath and R. Mock, Nucl. Instr. Meth. Phys **B34** (1988), 347.
25. D. Hinshelwood, G. Cooperstein, D. Mosher, D. Ponce, S. Strasburg, S. Swanekamp, S. Stephanakis, B. Weber, F. Young, A. Critchley, I. Crotch, and J. Threadgold, IEEE Trans. Plasma Sci. 33, 696 (2005).
26. J. Threadgold, I. Crotch, D. V. Rose, J. Maenchen, in 14th International Pulsed Power Conference **(PPC-2003),** 2003, M. Giesselman and A. Neuber, Eds., ISBN 0-7803-7915-2, 995-998.
27. P. N. Martin, J. R. Threadgold, S. Vickers, IEEE Trans. Plasma Sci. 41 (2013) 2510-2515.
28. D.W. Forster *et al*, *Electron beam diagnostics using x rays*, AWE Aldermaston, Tech. Rep. SSWA/JCM/714/162, April 1971.
29. T. J. Renk *et al*, RITS SMP manuscript in preparation.

FIGURE CAPTIONS

Fig. 1. Schematic diagram of the RITS-6 downstream MITL and SMP load region.

Fig. 2. Representative current (a) and voltage (b) waveforms, RITS Shot 1540.

Fig. 3. Schematic view of the RITS test chamber (top view): includes converter package, P-I-N detector locations, and materials between the photon source and the P-I-N locations attenuating the photon flux. (Drawing not to scale).

Fig. 4. Scaled axial (PIN_0) and 95° (PIN_95) signals, Shot 1540.

Fig. 5.a. Example of best-case power fit to CYLTRAN output, 70° electron angle, 95° detector. b. Worst-case fit, 80° electron angle, 0° detector.

Fig. 6.a. x-factors, power law, for detectors as function of electron angle. Coefficients as function of electron angle.

Fig. 7a. a. V_{CORR}_F and V_{CORR}_G plotted with (scaled) axial PIN_0, Shot 1780. b. Two solutions for V from Eq. 4, solved for electron angle assumptions of 20° and 30°, plotted against the V_{CORR}_G waveform from Shot 1780.

Fig. 8. (Normalized) PIN_95, PIN_45, and PIN_0, from Shot 1780.

Fig. 9. Two-piece V_{CORR}_G estimate for Shot 1780. The second piece is taken from the (falling) part of the 30° unfold estimate for V_{CORR}_G from Eq. 4.

Fig. 10. a. Scaled PIN_95, _PIN_45, _PIN_0 waveforms, Shot 1908. b. Three solutions for V from Eq. 4, solved for electron angle assumptions of 20°, 30°, and 40°, plotted against the V_{CORR}_G waveform from Shot 1908.

Fig. 11. Axial (scaled) PIN_0 and V_{CORR}_G waveforms, Shot 1540.

Fig. 12.a. Piece-wise V_{CORR}_G, Shot 1540, early in time, plotted against voltage inverts using PIN_0 and assuming 10°, 20°, 30° beam angles. B. Piece-wise V_{CORR}_G, Shot 1540, later in time, plotted against voltage unfolds using PIN_0 and assuming 20°, 30°, 40° beam angles.

Fig. 13. Composite cIV^x waveform, Shot 1540, plotted with (scaled) PIN_0/PIN_95.

Fig. 14. Scaled PIN_95, _PIN_45, _PIN_0 waveforms, Shot 1850.

Fig.15. a. Voltage contours from CYLTRAN output plotted in dose-rate space. b) Angle contours from CYLTRAN plotted in dose-rate space.

Fig. 16. a. Composite data plot, Shot 1780, with voltage contours. b) Composite data plot, Shot 1780, with angle contours.

Fig. 17. Composite data plot, Shot 1908, with angle contours.

Fig. 18.a. Composite data plot, Shot 1540, with voltage contours. b) Composite data plot, Shot 1540, with angle contours.

Fig. 19. Shot 1774 (scaled) dose-rate waveforms, PIN_0, PIN_45, PIN_95, plotted with (scaled) IBEAM current.

Fig. 20.a. Composite data plot, Shot 1774, with voltage contours. b) Composite data plot, Shot 1774, with angle contours.

Fig. 21.a. CYLTRAN voltage interpolation vs. V_{CORR}_G, Shot 1540. B) beam angle interpolation, Shot 1540.

Fig. 22.a. CYLTRAN voltage interpolation vs. V_{CORR}_G, Shot 1774. B) beam angle interpolation, Shot 1774.

FIGURES

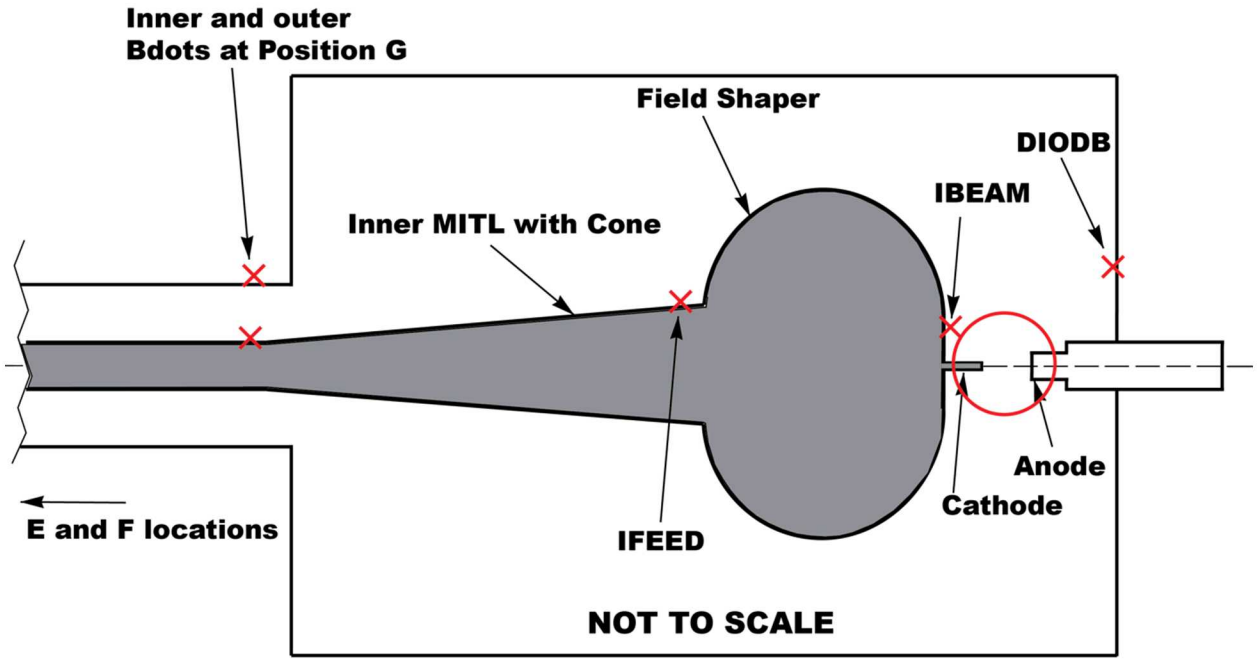

Fig. 1

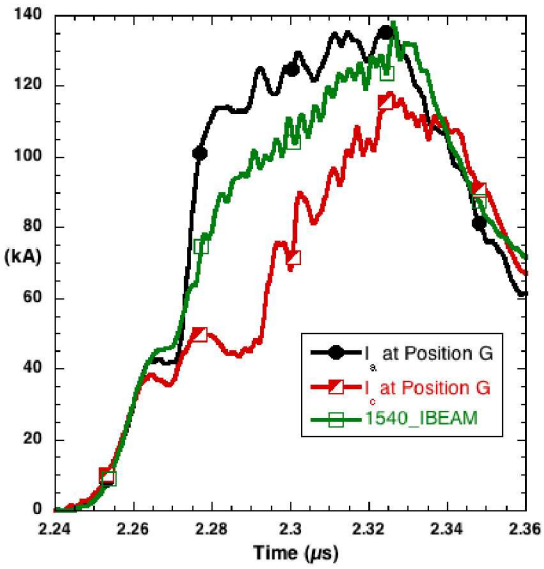
140
120
100
80
(kA)
60
40
20
0
2.24
2.26
2.28
2.3
2.32
2.34
2.36
Time (μs)
I_a at Position G
I_c at Position G
1540_IBEAM

Fig. 2a

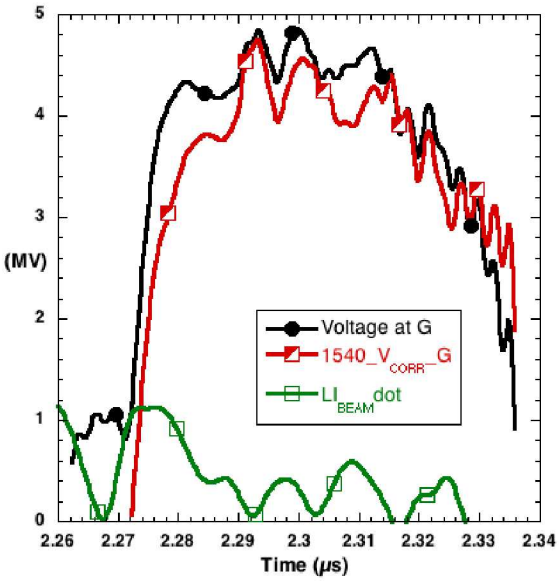
5
4
3
(MV)
2
1
0
2.26
2.27
2.28
2.29
2.3
2.31
2.32
2.33
2.34
Time (μs)
Voltage at G
1540_V_CORR_G
LI_BEAM dot

Fig. 2b

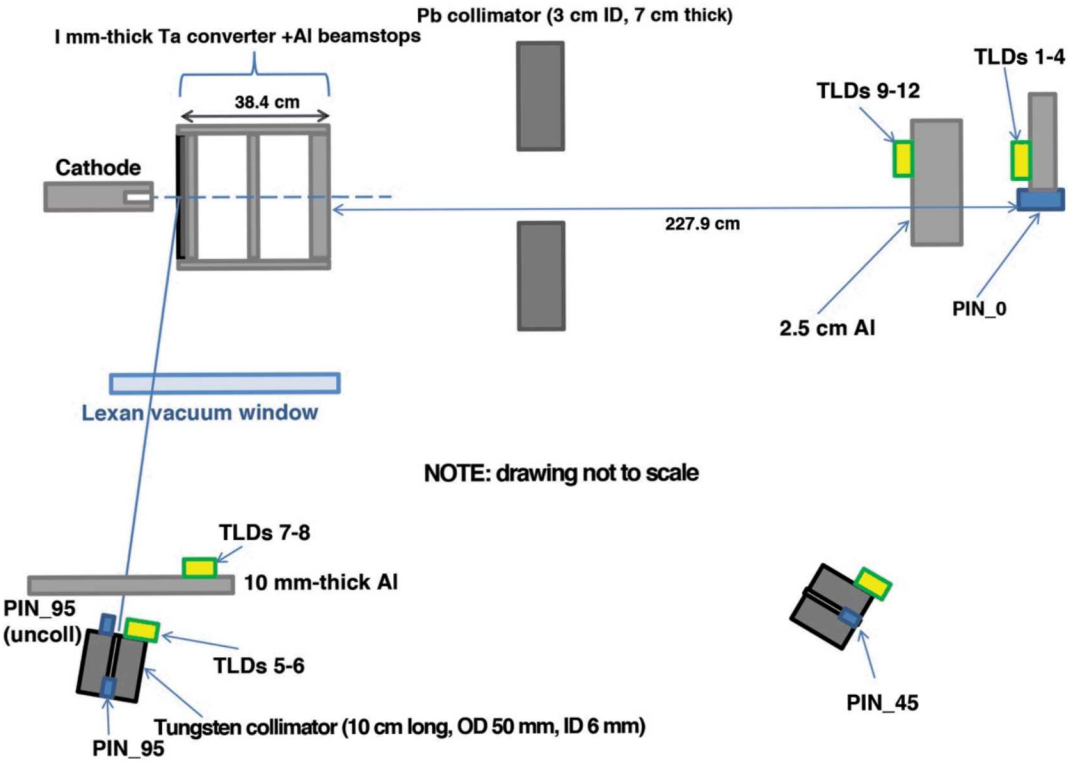
Pb collimator (3 cm ID, 7 cm thick)
1 mm-thick Ta converter +Al beamstops
38.4 cm
TLDs 1-4
TLDs 9-12
Cathode
227.9 cm
2.5 cm Al
PIN_0
Lexan vacuum window
NOTE: drawing not to scale
TLDs 7-8
10 mm-thick Al
PIN_95
(uncoll)
TLDs 5-6
Tungsten collimator (10 cm long, OD 50 mm, ID 6 mm)
PIN_95
PIN_45

Fig. 3

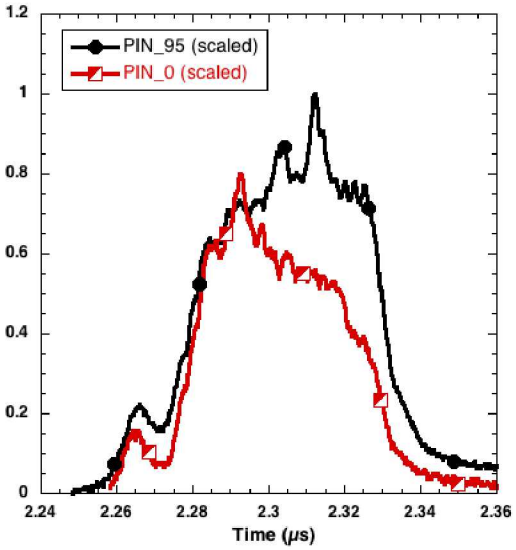
PIN_95 (scaled)
PIN_0 (scaled)
1.2
1
0.8
0.6
0.4
0.2
0
2.24
2.26
2.28
2.3
2.32
2.34
2.36
Time (μs)

Fig. 4

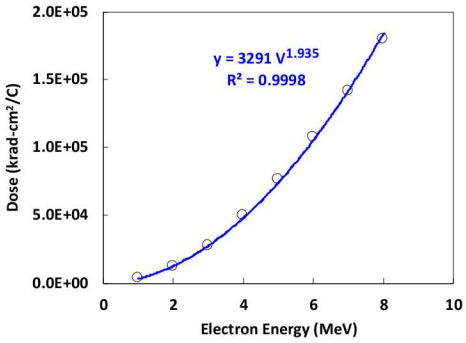
y = 3291 V^1.935
R² = 0.9998
Dose (krad-cm²/C)
Electron Energy (MeV)
2.0E+05
1.5E+05
1.0E+05
5.0E+04
0.0E+00
0
2
4
6
8
10

Fig. 5a

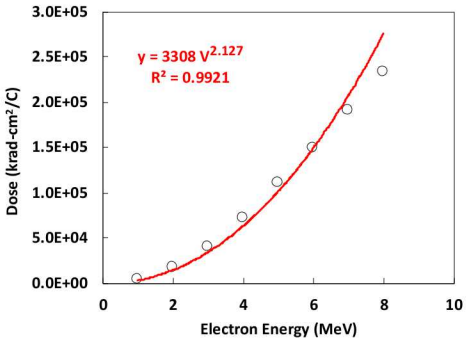
y = 3308 V^2.127
R² = 0.9921
Dose (krad-cm²/C)
Electron Energy (MeV)
3.0E+05
2.5E+05
2.0E+05
1.5E+05
1.0E+05
5.0E+04
0.0E+00
0
2
4
6
8
10

Fig. 5b

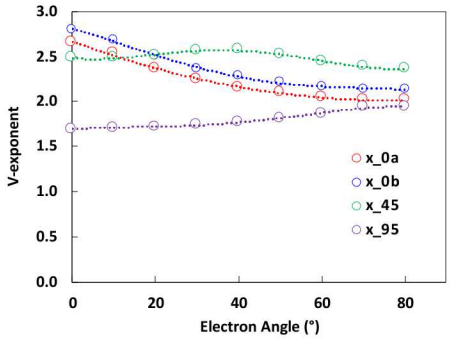
3.0
2.5
2.0
1.5
1.0
0.5
0.0
V-exponent
0
20
40
60
80
Electron Angle (°)
x_0a
x_0b
x_45
x_95

Fig. 6a

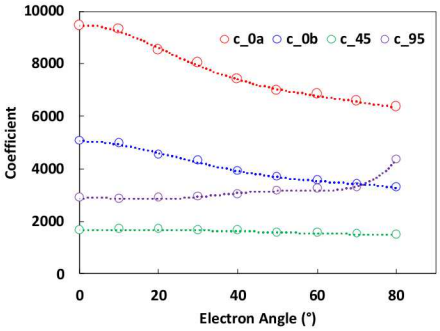
10000
8000
6000
4000
2000
0
Coefficient
0
20
40
60
80
Electron Angle (°)
c_0a
c_0b
c_45
c_95

Fig. 6b

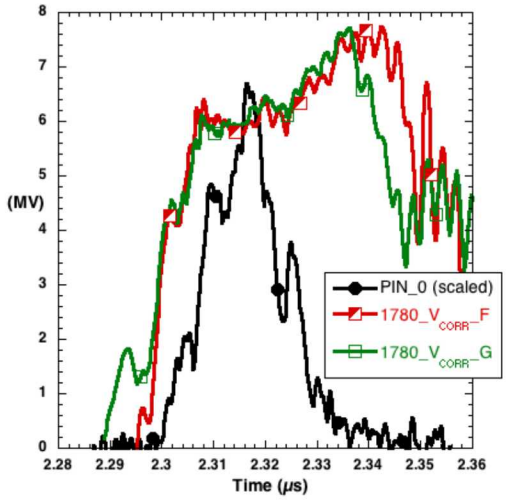
(MV)
Time (μs)
PIN_0 (scaled)
1780_V_CORR_F
1780_V_CORR_G

Fig. 7a

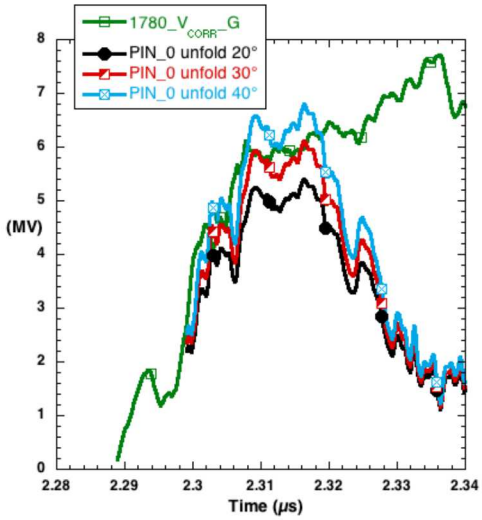
(MV)
Time (μs)
1780_V_CORR_G
PIN_0 unfold 20°
PIN_0 unfold 30°
PIN_0 unfold 40°

Fig. 7b

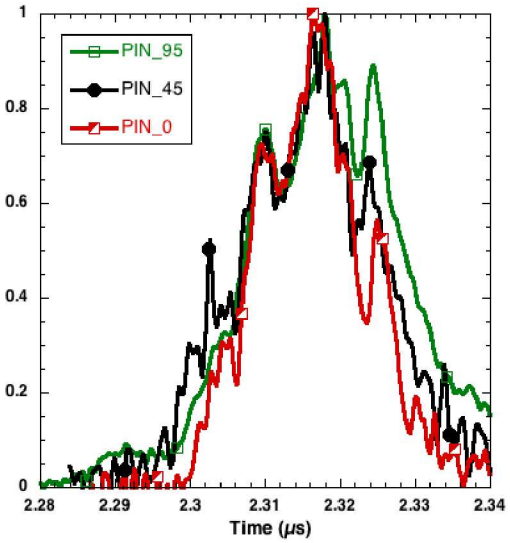
PIN_95
PIN_45
PIN_0
1
0.8
0.6
0.4
0.2
0
2.28
2.29
2.3
2.31
2.32
2.33
2.34
Time (μs)

Fig. 8

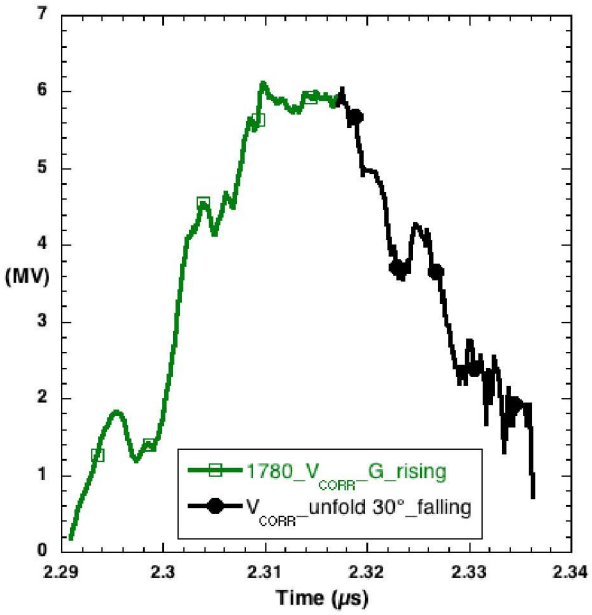
7
6
5
4
(MV)
3
2
1
0
2.29
2.3
2.31
2.32
2.33
2.34
Time (μs)
1780_V_CORR_G_rising
V_CORR_unfold 30°_falling

Fig. 9

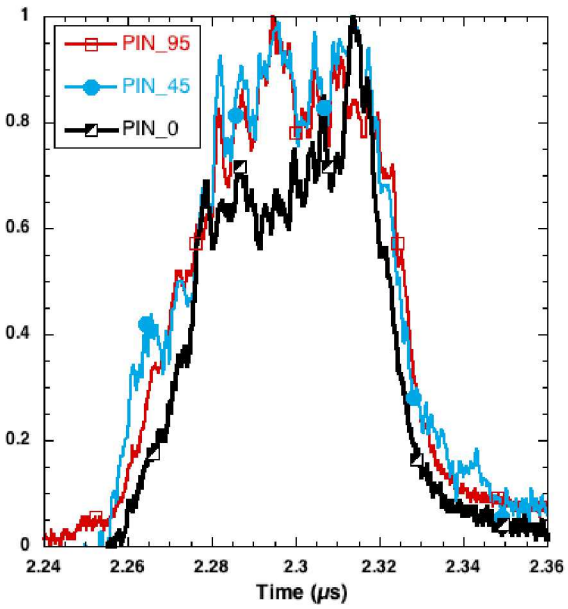

Fig. 10a

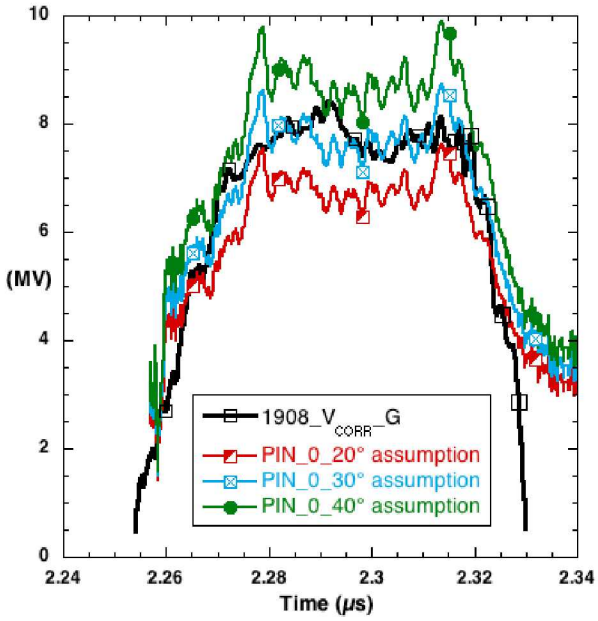

Fig. 10b

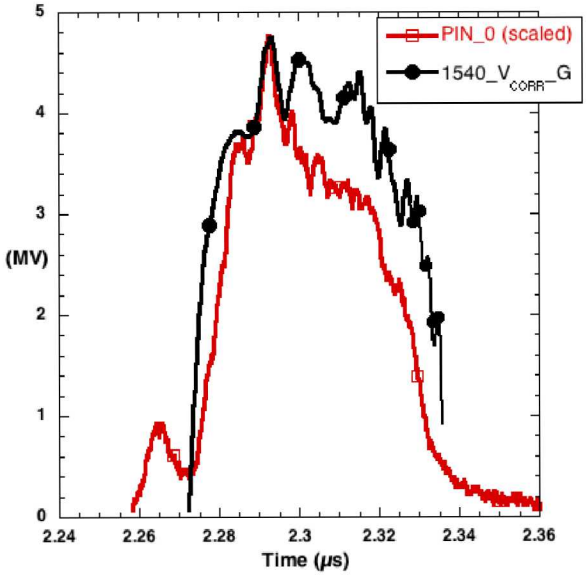
PIN_0 (scaled)
1540_V_CORR_G
(MV)
Time (μs)
0
1
2
3
4
5
2.24
2.26
2.28
2.3
2.32
2.34
2.36

Fig. 11

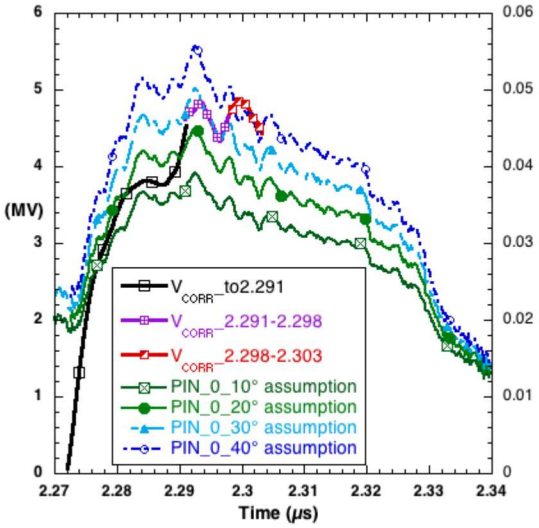

Fig. 12a

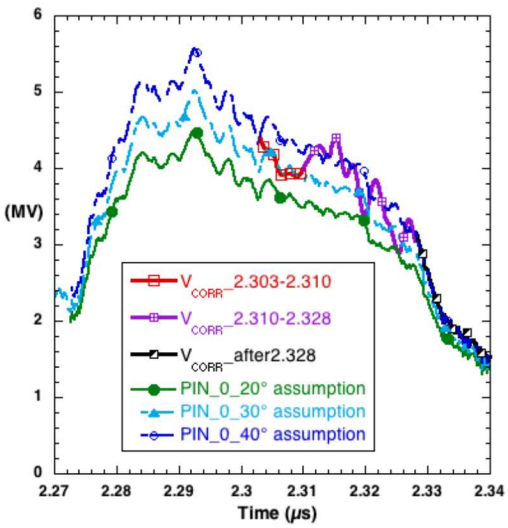

Fig. 12b

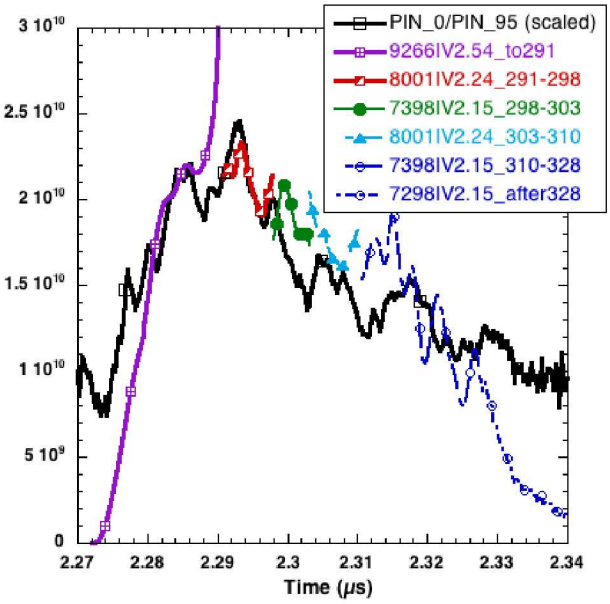
PIN_0/PIN_95 (scaled)
9266IV2.54_to291
8001IV2.24_291-298
7398IV2.15_298-303
8001IV2.24_303-310
7398IV2.15_310-328
7298IV2.15_after328
3 10^10
2.5 10^10
2 10^10
1.5 10^10
1 10^10
5 10^9
0
2.27
2.28
2.29
2.3
2.31
2.32
2.33
2.34
Time (μs)

Fig. 13

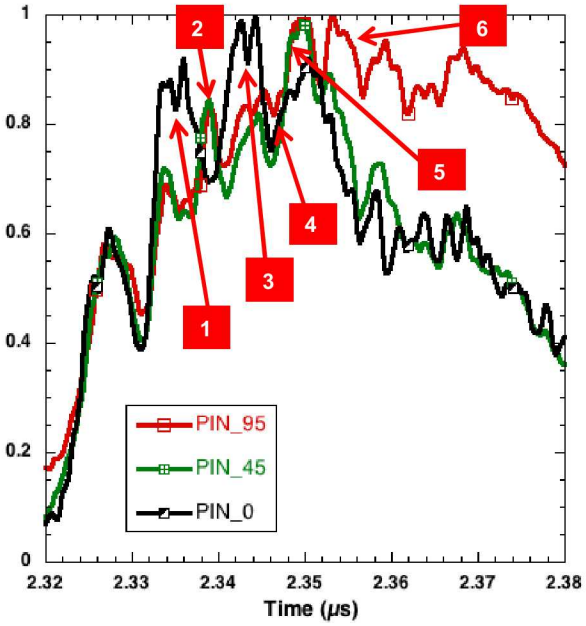
1
2
3
4
5
6
PIN_95
PIN_45
PIN_0
0
0.2
0.4
0.6
0.8
1
2.32
2.33
2.34
2.35
2.36
2.37
2.38
Time (μs)

Fig. 14

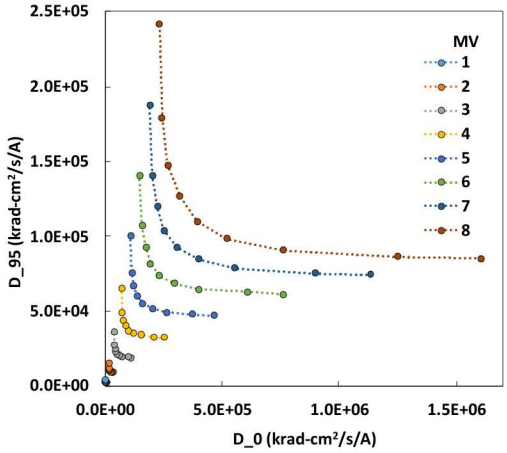

Fig. 15a

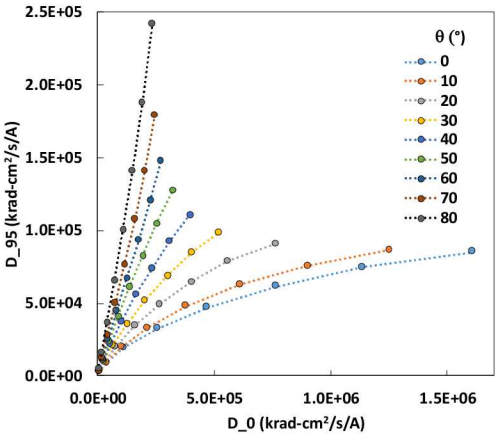

Fig. 15b

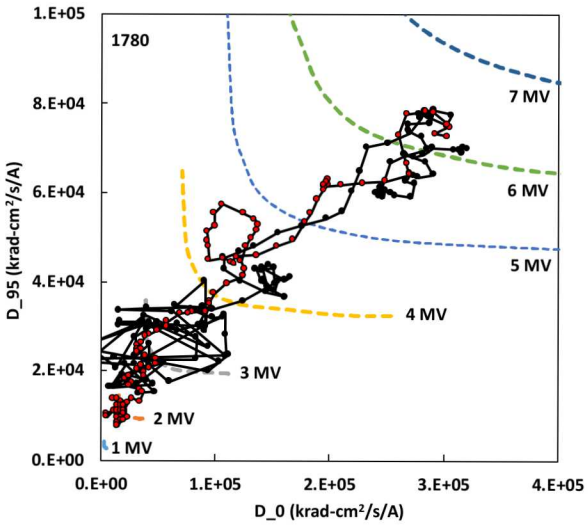

Fig. 16a

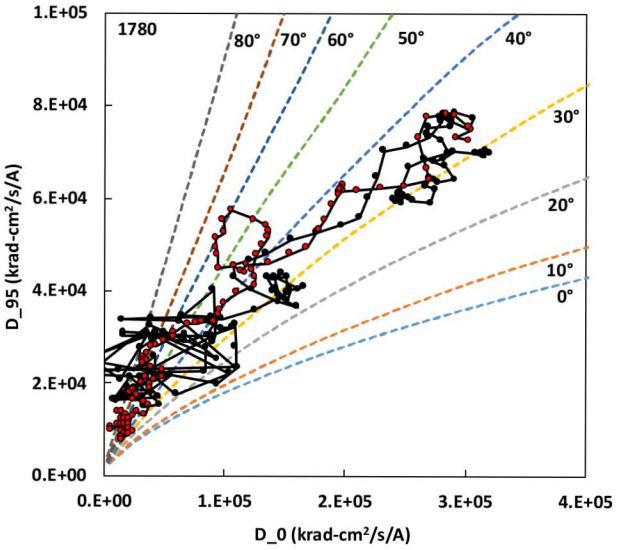

Fig. 16b

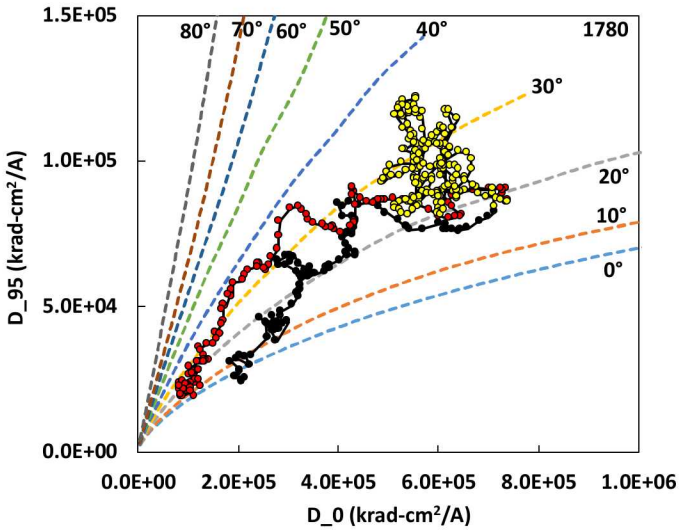
1.5E+05
1.0E+05
5.0E+04
0.0E+00
D_95 (krad-cm²/A)
0.0E+00
2.0E+05
4.0E+05
6.0E+05
8.0E+05
1.0E+06
D_0 (krad-cm²/A)
80°
70°
60°
50°
40°
30°
20°
10°
0°
1780

Fig. 17

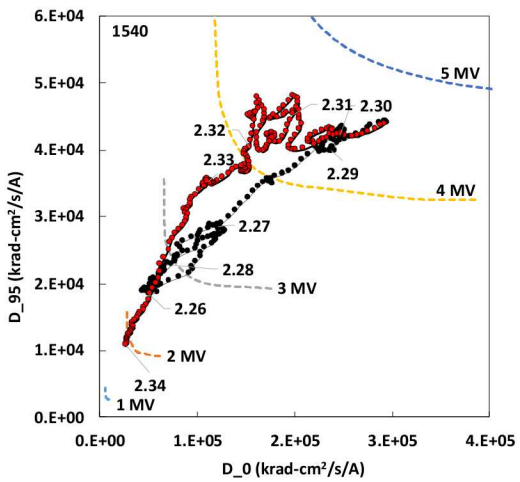

Fig. 18a

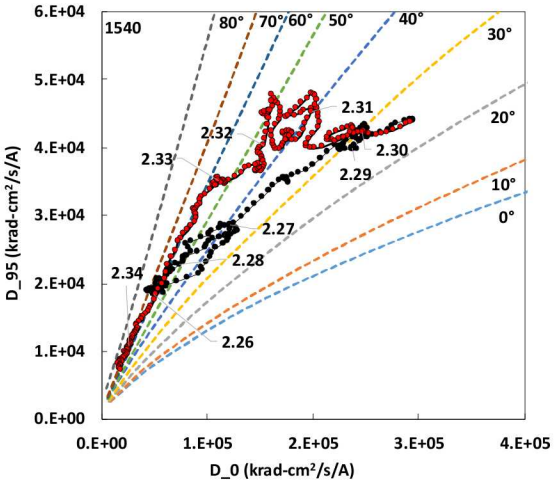

Fig. 18b

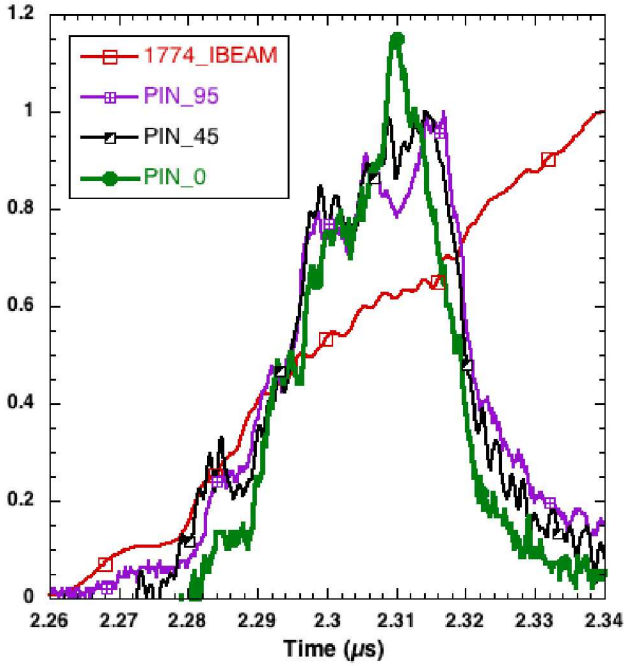
1774_IBEAM
PIN_95
PIN_45
PIN_0
1.2
1
0.8
0.6
0.4
0.2
0
2.26
2.27
2.28
2.29
2.3
2.31
2.32
2.33
2.34
Time (μs)

Fig. 19

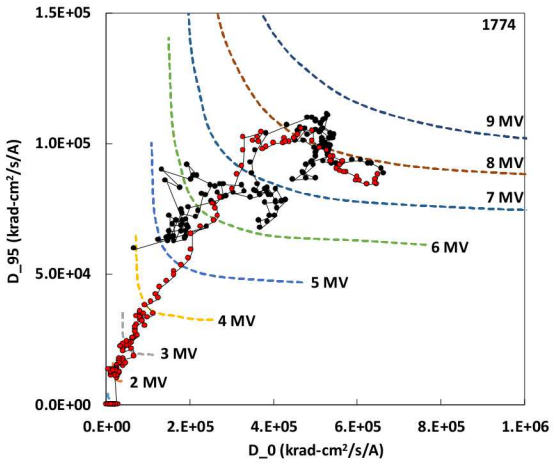

Fig. 20a

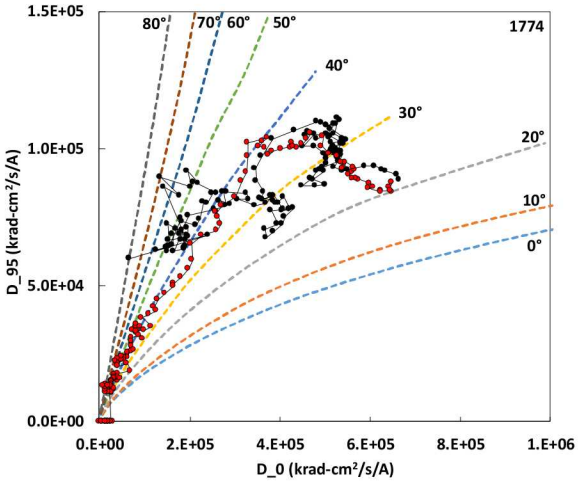

Fig. 20b

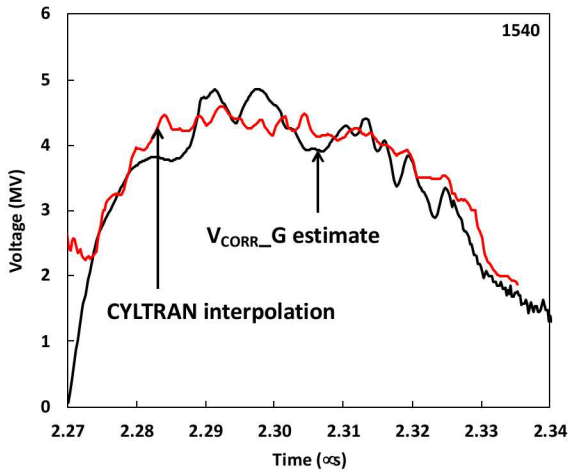

Fig. 21a

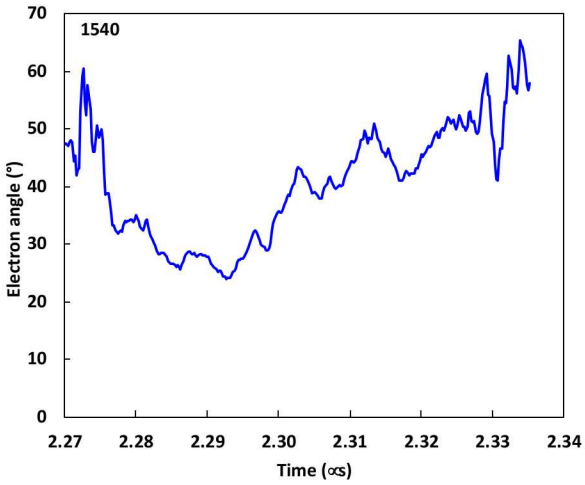

Fig. 21b

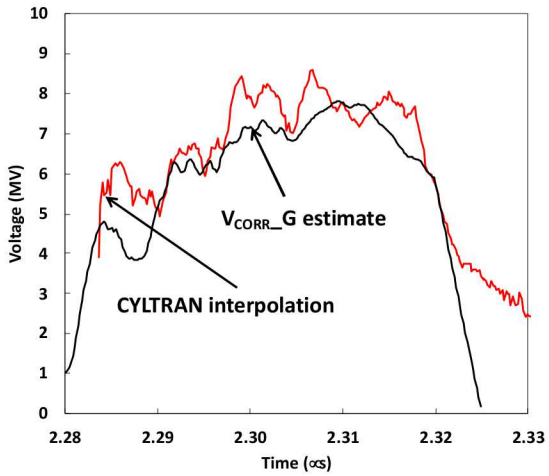

Fig. 22a

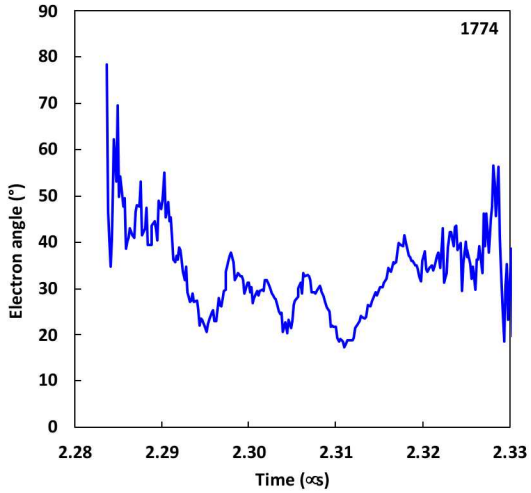

Fig. 22b